

The LOFAR Multifrequency Snapshot Sky Survey (MSSS)

I. Survey description and first results

G. H. Heald^{1,2}, R. F. Pizzo¹, E. Orrú¹, R. P. Breton³, D. Carbone⁴, C. Ferrari⁵, M. J. Hardcastle⁶, W. Jurusik⁷, G. Macario⁵, D. Mulcahy³, D. Rafferty⁸, A. Asgekar^{1*}, M. Brentjens¹, R. A. Fallows¹, W. Frieswijk¹, M. C. Toribio¹, B. Adebahr⁸, M. R. Bell⁹, A. Bonafede⁸, J. Broderick^{3,10}, Y. Cendes⁴, A. O. Clarke³, J. Croston³, F. de Gasperin¹¹, J. Gregson¹², J. Harwood^{1,6}, V. Heesen³, A. J. van der Horst⁴, V. Jelic^{2,1}, D. Jones¹³, J. P. McKean^{1,2}, B. Nikiel-Wroczyński⁷, M. Pandey-Pommier¹⁴, M. Pietka^{3,10}, C. Riseley³, A. Rowlinson¹⁵, J. Sabater¹⁶, A. M. M. Scaife³, L. H. A. Scheers¹⁷, K. Sendlinger¹⁸, A. Shulevski², C. Sobey¹, A. J. Stewart^{10,3}, A. Stroe¹⁹, J. Swinbank⁴, C. Tasse^{20,21,22}, J. Trüstedt^{23,24}, E. Varenius²⁵, N. Vilchez¹, R. J. van Weeren²⁶, S. Wijnholds¹, additional MSSS team members, A. G. de Bruyn^{1,2}, R. Nijboer¹, M. Wise¹ and LOFAR Builders List

¹ Netherlands Institute for Radio Astronomy (ASTRON), Postbus 2, 7990 AA Dwingeloo, The Netherlands

² Kapteyn Astronomical Institute, University of Groningen, PO Box 800, 9700 AV, Groningen, The Netherlands

³ School of Physics and Astronomy, University of Southampton, SO17 1BJ, UK

⁴ Anton Pannekoek Institute, University of Amsterdam, Postbus 94249, 1090 GE Amsterdam, The Netherlands

⁵ Laboratoire Lagrange, UMR 7293, Université de Nice Sophia-Antipolis, CNRS, Observatoire de la Côte d'Azur, 06300 Nice, France

⁶ School of Physics, Astronomy and Mathematics, University of Hertfordshire, College Lane, Hatfield AL10 9AB, UK

⁷ Astronomical Observatory, Jagiellonian University, ul. Orla 171, 30-244, Kraków, Poland

⁸ Max-Planck-Institut für Radioastronomie, Auf dem Hügel 69, 53121, Bonn, Germany

⁹ Max Planck Institute for Astrophysics, Karl-Schwarzschild-Str. 1, 85748, Garching, Germany

¹⁰ Astrophysics, University of Oxford, Denys Wilkinson Building, Keble Road, Oxford OX1 3RH, UK

¹¹ Universität Hamburg, Hamburger Sternwarte, Gojenbergsweg 112, 21029, Hamburg, Germany

¹² Department of Physics & Astronomy, The Open University, Milton Keynes MK7 6AA, UK

¹³ IMAPP/Department of Astrophysics, Radboud University, PO Box 9010, 6500 GL, Nijmegen, The Netherlands

¹⁴ CRAL, Observatoire de Lyon, Université Lyon 1, 9 Avenue Ch. André, 69561 Saint Genis Laval Cedex, France

¹⁵ CSIRO Astronomy and Space Science, PO Box 76, Epping, NSW 1710, Australia

¹⁶ Institute for Astronomy (IfA), University of Edinburgh, Royal Observatory, Blackford Hill, Edinburgh EH9 3HJ, UK

¹⁷ Centrum Wiskunde & Informatica, P.O. Box 94079, 1090 GB Amsterdam, The Netherlands

¹⁸ Astronomisches Institut der Universität Bochum, Universitätsstr. 150, 44801 Bochum, Germany

¹⁹ Leiden Observatory, Leiden University, NL-2300 RA Leiden, the Netherlands

²⁰ GEPI, Observatoire de Paris, CNRS, Université Paris Diderot, 5 place Jules Janssen, 92190, Meudon, France

²¹ SKA South Africa, 3rd Floor, The Park, Park Road, 7405, Pinelands, South Africa

²² Department of Physics & Electronics, Rhodes University, PO Box 94, 6140, Grahamstown, South Africa

²³ Dr. Remeis Sternwarte & ECAP, Universität Erlangen-Nürnberg, Sternwartstrasse 7, 96049, Bamberg, Germany

²⁴ Institut für Theoretische Physik und Astrophysik, Universität Würzburg, Emil-Fischer-Str. 31, 97074, Würzburg, Germany

²⁵ Department of Earth and Space Sciences, Chalmers University of Technology, Onsala Space Observatory, 439 92 Onsala, Sweden

²⁶ Harvard-Smithsonian Center for Astrophysics, 60 Garden Street, Cambridge, MA 02138, USA

Preprint online version: October 7, 2014

ABSTRACT

We present the Multifrequency Snapshot Sky Survey (MSSS), the first northern-sky LOFAR imaging survey. In this introductory paper, we first describe in detail the motivation and design of the survey. Compared to previous radio surveys, MSSS is exceptional due to its intrinsic multifrequency nature providing information about the spectral properties of the detected sources over more than two octaves (from 30 to 160 MHz). The broadband frequency coverage, together with the fast survey speed generated by LOFAR's multibeaming capabilities, make MSSS the first survey of the sort anticipated to be carried out with the forthcoming Square Kilometre Array (SKA). Two of the sixteen frequency bands included in the survey were chosen to exactly overlap the frequency coverage of large-area Very Large Array (VLA) and Giant Metrewave Radio Telescope (GMRT) surveys at 74 MHz and 151 MHz respectively. The survey performance is illustrated within the "MSSS Verification Field" (MVF), a region of 100 square degrees centered at $(\alpha, \delta)_{J2000} = (15^h, 69^\circ)$. The MSSS results from the MVF are compared with previous radio survey catalogs. We assess the flux and astrometric uncertainties in the catalog, as well as the completeness and reliability considering our source finding strategy. We determine the 90% completeness levels within the MVF to be 100 mJy at 135 MHz with 108'' resolution, and 550 mJy at 50 MHz with 166'' resolution. Images and catalogs for the full survey, expected to contain 150,000 – 200,000 sources, will be released to a public web server. We outline the plans for the ongoing production of the final survey products, and the ultimate public release of images and source catalogs.

Key words. Surveys — Radio continuum: general

1. Background

All-sky continuum surveys are a key application of radio telescopes. They provide the only unbiased view of galaxies in the Universe, enable searches for rare sources, and provide a pathway for the discovery of new phenomena. Several large-area surveys have been performed with existing radio telescopes at a number of frequencies. Among these, many of the earliest were performed at low frequencies ($\nu \lesssim 350$ MHz) (see e.g. Jauncey 1975). The new Low Frequency Array (LOFAR; van Haarlem et al. 2013) operates at frequencies between 10 and 240 MHz, and was constructed with one primary aim being to perform groundbreaking imaging surveys of the Northern sky (Röttgering et al. 2011). Currently, the most extensive low frequency catalogs at or near LOFAR frequencies are the Eighth Cambridge Survey of Radio Sources (8C; Rees 1990, catalog revised by Hales et al. 1995), the VLA Low-Frequency Sky Survey (VLSS; Cohen et al. 2007, and the revised catalog VLSSr; Lane et al. 2012), the Seventh Cambridge Survey of Radio Sources (7C; Hales et al. 2007), the Westerbork Northern Sky Survey (WENSS; Rengelink et al. 1997), and most recently the Murchison Widefield Array (MWA; Tingay et al. 2013) Commissioning Survey (MWACS; Hurley-Walker et al. 2014). Other ongoing low-frequency radio surveys include the TIFR GMRT Sky Survey (TGSS¹) that is using the Giant Metrewave Radio Telescope (GMRT) and has already released survey data products to the community, and the Galactic and Extragalactic MWA Survey (GLEAM).

A key application of all-sky radio surveys is the comparison of source properties at the wide range of frequencies at which they are detected. This provides crucial information from which the physical properties of these sources can be derived.

To date, no wide-area radio surveys have been performed with large fractional bandwidth (i.e., 2:1 or more). This situation is bound to change in the era of the Square Kilometre Array (SKA; Carilli & Rawlings 2004). The SKA and its pathfinder and precursor projects plan wide-area surveys of radio continuum sources, with large fractional bandwidth. This opens the door for the spectral study of sources detected within the survey, using only the survey data itself. LOFAR is a key SKA pathfinder telescope (van Haarlem et al. 2013) in the 10 and 240 MHz frequency range. The array is centered in the Netherlands with outlying stations in Germany, France, the United Kingdom, and Sweden. LOFAR is built up from thousands of dipoles clustered in groups called stations. The signals from the dipoles making up each station are digitally combined to steer the beam in one or more directions of interest. Stations are combined in a software correlator located in Groningen, a city in the north of the Netherlands. One of the key applications of LOFAR is wide-field imaging. In this paper we introduce a new radio survey performed with LOFAR, the Multifrequency Snapshot Sky Survey (MSSS), that has been driven forward as a commissioning project for the telescope. The MSSS project serves as a testbed for operations – particularly large-scale imaging projects – and enables straightforward processing of later observations.

The motivations for performing MSSS and the design of the survey are described in detail in § 2. The calibration and imaging strategies are presented § 3, and the resulting standard data products are described in § 4. We illustrate the performance of

the survey through a detailed analysis of the “MSSS Verification Field” (MVF) in § 5. Several avenues for scientific exploitation of MSSS are outlined in § 6, and we conclude the paper in § 7.

2. Context and survey design

Imaging applications with the LOFAR telescope will require automated processing. The calibration step in particular needs to be largely unattended, with a major implication that *a priori* sky models are required at arbitrary locations on the sky. A number of northern sky radio surveys are available in the literature, but do not cover the proper frequency range at the resolution needed to reliably initiate calibration routines. Moreover, a coherent commissioning project was required to focus development activities and produce a generic automated processing pipeline, while simultaneously exercising the end-to-end telescope operations. These goals led to the initiation of the “Multifrequency Snapshot Sky Survey” (MSSS)².

In the original MSSS plans (early 2008), it was anticipated that the survey would be performed using 13 core stations (CS), 7 remote stations (RS), and 3 international stations (EU). Ultimately, the array construction proceeded rapidly, and MSSS has been performed with the full complement of stations (except in HBA, where the international stations were unused due to correlator limitations at the time of the observations). This leads to a significantly different array than originally envisioned, both in terms of sensitivity and *uv* coverage. A complete overview of the LOFAR system is provided by van Haarlem et al. (2013). The telescope layout, as well as processing software limitations (now substantially reduced), led to plans for a low-resolution survey initially, with aspirations for a higher resolution survey in future.

The MSSS survey effort needs to provide images and catalogs with sufficient angular resolution to reliably initiate the self-calibration cycle in the imaging pipeline. At the same time, the frequency coverage needs to be sufficient to ensure that spectral variations within the model are accounted for. These requirements were balanced with the need for a relatively rapid survey, taking on the order of weeks of telescope time to perform.

With all of these considerations in mind, we designed a two-component observational strategy. The Low Band Antenna (LBA) component covers the 30 – 75 MHz range, and the High Band Antenna (HBA) component covers the 119 – 158 MHz range. The exact frequencies were chosen to evenly cover the LBA range, and to avoid major RFI in the HBA range (see Table 1). The number of frequency bands (eight 2 MHz bands in each of the LBA and HBA components) were chosen to allow multiplexing the sky coverage. In early survey test observations, the “16-bit” correlator mode allowed three fields to be observed simultaneously, each with 16 MHz bandwidth. Near the end of 2012 (when most of the LBA test observations were complete, and test HBA observations were beginning), the “8-bit” correlator mode became available, doubling the number of fields that can be simultaneously observed (each with 16 MHz bandwidth) to six. The key parameters for the two frequency components of the survey are summarized in Table 1, and the setup of these are described in turn below.

Send offprint requests to: G. Heald, e-mail: heald@astron.nl

* Presently at Shell Technology Center, Bangalore 560048

¹ <http://tgss.ncra.tifr.res.in/150MHz/tgss.html>

² The original name of the survey was the “Million Source Shallow Survey”. Under current projections (see § 5), we expect to catalog well over 10^5 sources, but probably not 10^6 .

2.1. Setup of MSSS-LBA

The LBA component of MSSS is observed using the LBA_INNER configuration. In this mode, the digital station beams are formed using signals from the inner 48 dipoles of each 96-dipole station. The resulting compact station, with diameter $D = 32.25$ m, provides a large field of view. International stations are included in all MSSS-LBA observations in addition to the Dutch stations, and these come with the full complement of 96 dipoles. The LBA survey pointings were designed using a nominal primary beam half-power beam width (HPBW) at 60 MHz of 11.55 deg (from $\text{HPBW} = \alpha_b \lambda / D$, using $\alpha_b = 1.3$ and $\lambda = 5$ m). We now know that the appropriate value of $\alpha_b = 1.10 \pm 0.02$ (van Haarlem et al. 2013), so the station beams are 15% smaller than initially anticipated, and a somewhat larger variation in image noise across the survey can therefore be expected. This will be far less evident at MSSS-LBA frequencies lower than 60 MHz, where the beam sizes are much larger. Survey fields are laid out on strips of constant declination, and spaced equally on each strip by $\Delta\alpha \leq \text{HPBW}/2$. The declination strips are themselves separated by $\Delta\delta = \text{HPBW}/2$. This results in a total of 660 MSSS-LBA fields.

Initial tests, performed before the station digital beam forming was properly calibrated, indicated that interleaving calibrator observations between target observations would not lead to a sufficiently stable amplitude scale (see § 3 for details of the calibration strategy). Thus, we adopted an observing mode wherein one of the primary calibrators is always observed, using the identical 16 MHz bandwidth, in parallel with two simultaneous target field observations (or five target fields, when 8-bit mode is used).

The amount of observing time used per field is based on the goal of obtaining image noise at the 10 mJy beam^{-1} level, in each of the eight 2 MHz bands. Using early projections of the image sensitivity expected from LOFAR, an estimate of 90 minutes per field was obtained. To improve uv coverage (see below) this was split up into 9 snapshots. The start times of the individual snapshots are spaced by 1 hr for northern target fields ($\delta > 30^\circ$), and by 45 min for target fields closer to the celestial equator ($\delta < 30^\circ$). The central (fifth) snapshot is observed near transit ($\text{HA} \approx 0$ hr). For ease of scheduling, the final survey observing time per field is $9 \times 11 = 99$ min, yielding initially estimated theoretical thermal noise values between about 6 – 20 mJy beam^{-1} depending on band.

From observations of calibrator sources, we now have empirical estimates of the LOFAR station System Equivalent Flux Densities (SEFDs); these are provided by van Haarlem et al. (2013). Based on those numbers we can see that an observing time of 99 min yields an expected thermal noise between about 5 – 10 mJy beam^{-1} . It should be noted however that the rudimentary calibration procedures that are implemented in the MSSS pipeline limit our actual sensitivity to an image noise that is typically a factor of a few higher than the thermal noise estimate. Moreover, classical confusion noise would likely limit images produced at the limited angular resolution targeted for default MSSS imaging (out to uv distance of 2 – $3k\lambda$), see Fig. 1. We calculate the expected confusion noise in two ways. The first is based on extrapolation from VLSS C-configuration estimates of the confusion noise (see Cohen 2004):

$$\sigma_{\text{conf,VLSS}} = 29 \left(\frac{\theta}{1''} \right)^{1.54} \left(\frac{\nu}{74 \text{ MHz}} \right)^{-0.7} \mu\text{Jy beam}^{-1}, \quad (1)$$

where θ is the synthesized beamsize, ν is the observing frequency, and we have extrapolated the VLSS estimate using a typical spectral index of -0.7 . The second estimate is from Condon

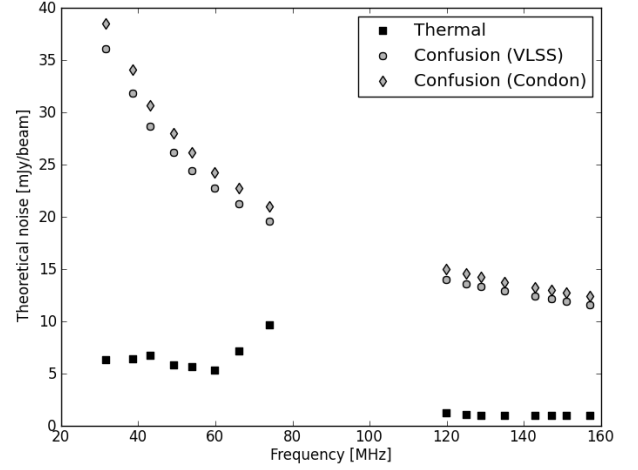


Fig. 1. Theoretical thermal and confusion noise per band for MSSS observations. The values take into account empirically-determined SEFD values from van Haarlem et al. (2013), and a uv distance cutoff of $3k\lambda$.

et al. (2012), who use deep VLA C-configuration observations at S-band (2 – 4 GHz) to derive

$$\sigma_{\text{conf,Condon}} = 1.2 \left(\frac{\theta}{8''} \right)^{10/3} \left(\frac{\nu}{3.02 \text{ GHz}} \right)^{-0.7} \mu\text{Jy beam}^{-1}. \quad (2)$$

We consider the numbers predicted for MSSS fairly reliable since the two estimates provide very similar values (on average only 6.4% different across the full MSSS frequency range) despite being based on data from very different observing frequencies and angular resolution.

The uv coverage obtained by splitting the observations of LBA fields into 9 snapshots is illustrated in Figure 2. The figure was created using the observations described in § 5.

Including overheads, the total amount of observing time required to complete MSSS-LBA (assuming 8-bit mode) is 297 hr. Approximately 130 TB of raw visibility data is collected by observing all 660 pointings and associated calibrator scans.

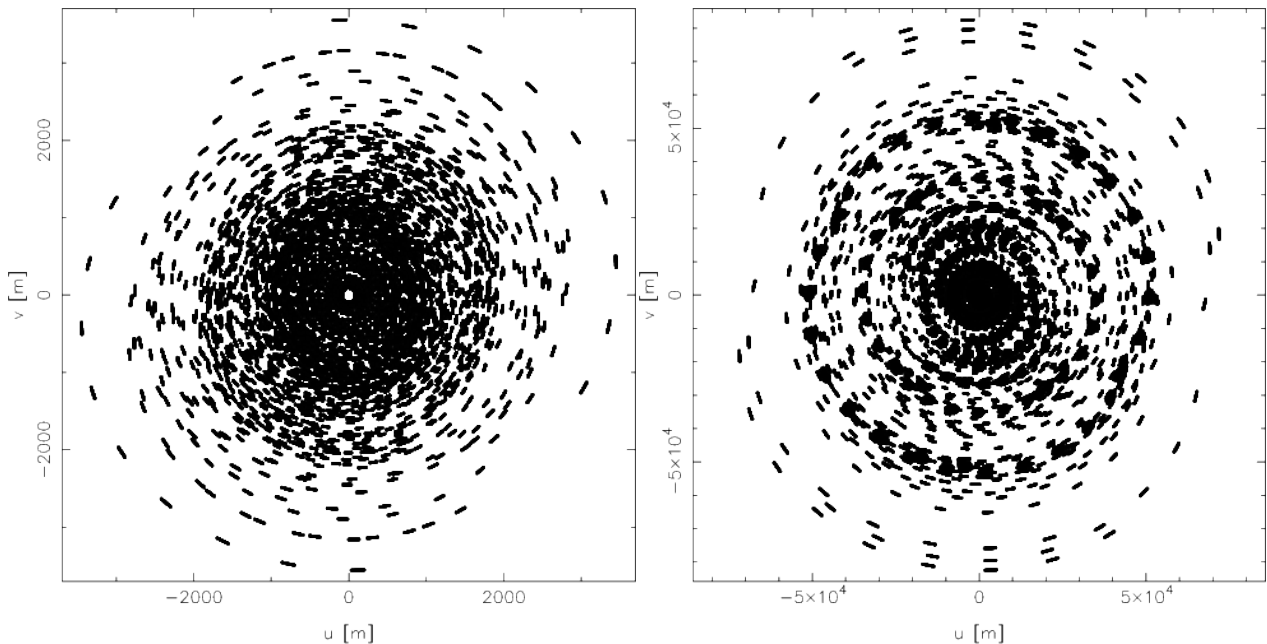
During the LBA portion of the survey, a single subband (bandwidth 195 kHz) centered at 60 MHz is always placed on the north celestial pole (NCP) as part of a transient and variability monitoring campaign coordinated by the LOFAR Transients Key Project. We return to this feature of the survey setup in § 6.

2.2. Setup of MSSS-HBA

The HBA component of MSSS is observed using the HBA_DUAL_INNER station configuration. In this mode, both 24-tile substations are utilized separately for each of the core stations. The outer 24 tiles of the 48-tile remote stations are disabled so that the field of view of the stations are all identical (at a small cost in sensitivity on the longer baselines van Haarlem et al. 2013). The survey pointings were designed using a nominal beam size at 150 MHz of $\text{HPBW} = 4.84$ deg (using $\alpha_b = 1.3$, $\lambda = 2$ m and $D = 30.75$ m). As in the LBA portion of the survey, our understanding of the station beam sizes has now been empirically determined to be smaller ($\alpha_b = 1.02 \pm 0.01$ for HBA core stations; van Haarlem et al. 2013). International stations are not included in the HBA portion of the survey, because at the time of observations the system had restrictions on the number of correlator inputs, requiring the loss of core stations when international stations were included. Since MSSS is primarily a low angular resolution survey, we kept the full complement of

Table 1. LOFAR MSSS configuration

Parameter	MSSS-LBA	MSSS-HBA
Station configuration	LBA_INNER	HBA_DUAL_INNER
Band central frequencies (MHz)	31, 37, 43, 49, 54, 60, 66, 74	120, 125, 129, 135, 143, 147, 151, 157
Calibrator observation type	Simultaneous	Serial
Calibrator observation time (min)	11	1
Observing time per snapshot (min)	11	7
Number of snapshots	9	2
Snapshot gap (h)	1 ($\delta > 30^\circ$) 0.75 ($\delta < 30^\circ$)	4
Number of fields	660	3616
Total survey time with overheads (hr)	297	201

**Fig. 2.** The uv coverage for the MSSS-LBA field L227+69, core only (left) and all Dutch stations (right).

core stations in the survey observations. A separate and complementary survey including the international stations has been conducted to search a representative portion of the LOFAR HBA sky for compact ($\lesssim 1''$) calibrators (Moldon 2014).

With the HBA observations, a simultaneous calibrator strategy as implemented in MSSS-LBA is not required, since the stability is much better. Moreover, such a strategy would not be possible, because the analog beamformer in each of the 16-dipole tiles reduces the field of view to approximately $\text{HPBW}_{\text{tile}} = \lambda/D_{\text{tile}} = 22.9 \text{ deg}$ (where $D_{\text{tile}} = 5 \text{ m}$ is the tile size) at 150 MHz. Thus, most field observations would not be able to include a parallel primary calibrator observation with sufficient sensitivity. Calibrator observations are therefore performed between field observations, using the same bandwidth as the field observations.

Similar sensitivity considerations as for the LBA component of MSSS led to a required observing time per HBA field of approximately 15 min. Snapshots are also used for HBA observations to somewhat improve uv coverage. Two snapshots are used, with the start times of the snapshots separated by 4 hr (bracketing transit, such that the hour angles of the snapshots are $\text{HA} \approx \pm 2 \text{ hr}$). For ease of scheduling we adopted $2 \times 7 \text{ min}$ per field. This leads to an estimated thermal noise of about 1 mJy beam^{-1} per band, using the empirical SEFD values given by van Haarlem et al. (2013). As with the LBA sensitivity, the

actual noise level in HBA images will be a factor of a few higher than the thermal noise estimate, and confusion is likely the true limiting factor in images with limited angular resolution, see Fig. 1.

The uv coverage of the two snapshot HBA observing strategy is shown in Figure 3. The survey grid was designed in the same way as the LBA grid, using $\text{HPBW} = 4.84 \text{ deg}$. The HBA component of MSSS is made up of 3616 fields. Including overheads, the total amount of observing time required to complete MSSS-HBA (assuming 8-bit mode) was 201 hr. Approximately 470 TB of raw visibility data is collected by observing all 3616 pointings and associated calibrator scans.

2.3. Survey fields

The layout of the MSSS survey fields was determined in such a way as to provide nearly uniform coverage at the optimized frequencies 60 MHz (MSSS-LBA) and 150 MHz (MSSS-HBA), as described in § 2.1 and 2.2. The coordinates of the center of the survey fields are shown on an Aitoff projection in Figure 4.

The MSSS fields planned and observed so far have a lower declination limit of $\delta = 0^\circ$. At a later date, the lower declination limit may be extended farther to the south, extending the MSSS sky coverage.

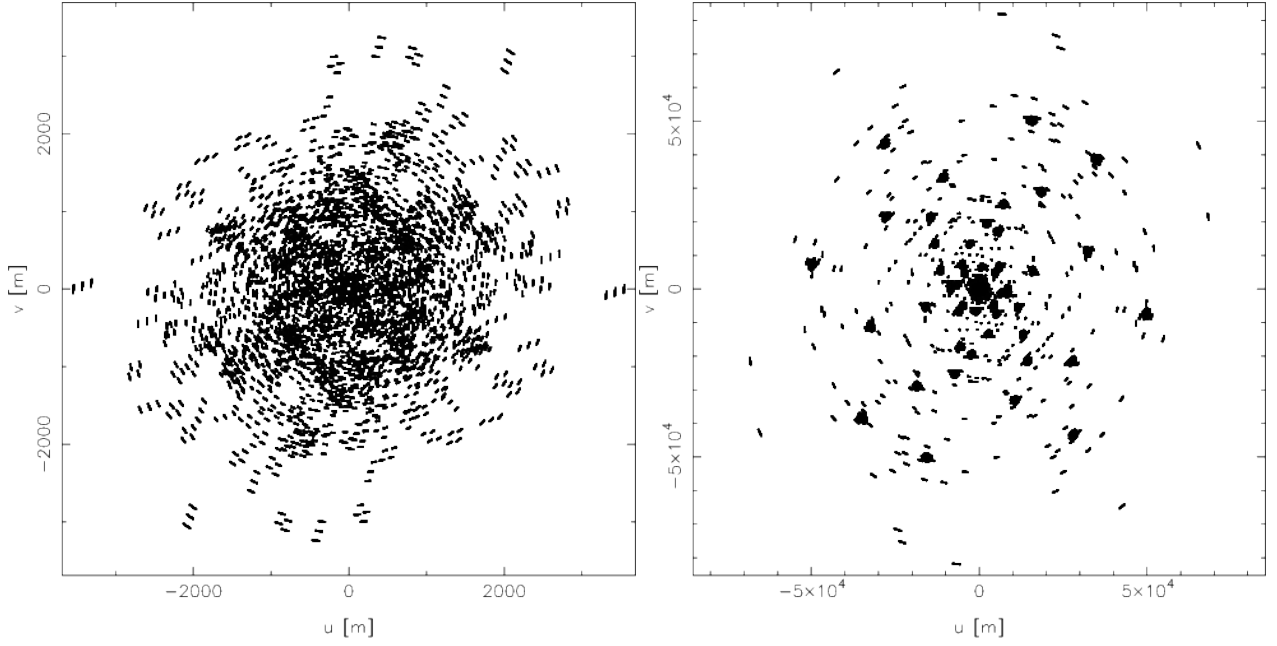


Fig. 3. The uv coverage for the MSSS-HBA field H229+70, core only (left) and all Dutch stations (right).

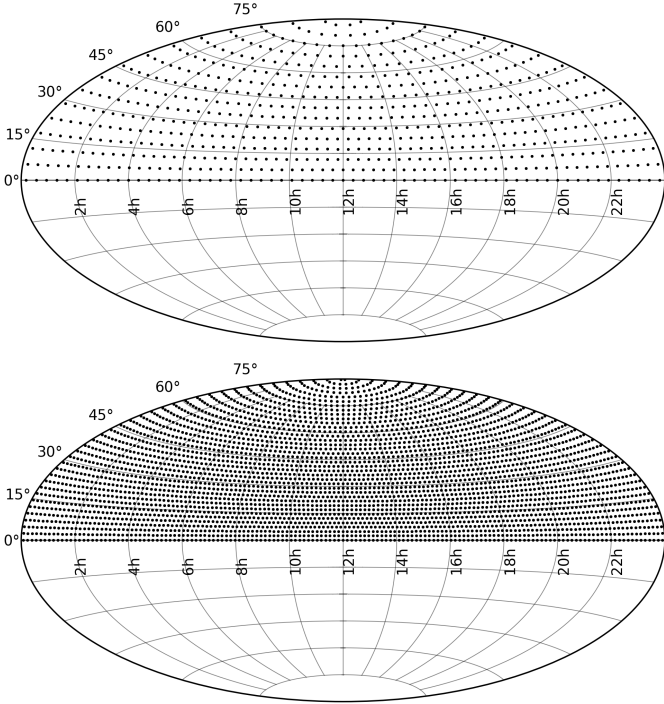


Fig. 4. MSSS fields for the LBA (*top*) and HBA (*bottom*) portions of the survey, presented in equatorial coordinates on an Aitoff projection. The LBA survey consists of 660 fields, while the HBA survey consists of 3616 fields.

2.4. Survey mosaics

The final presentation of the survey images (and derivation of the resulting catalog) will be based on $10^\circ \times 10^\circ$ mosaics generated from the individual HBA and LBA fields. The mosaic grid is common for both bands in order to facilitate multi-frequency flux comparison of sources detected in the survey. The survey contains a total of 220 mosaic fields, including one NCP mosaic centered at $\delta = 90^\circ$.

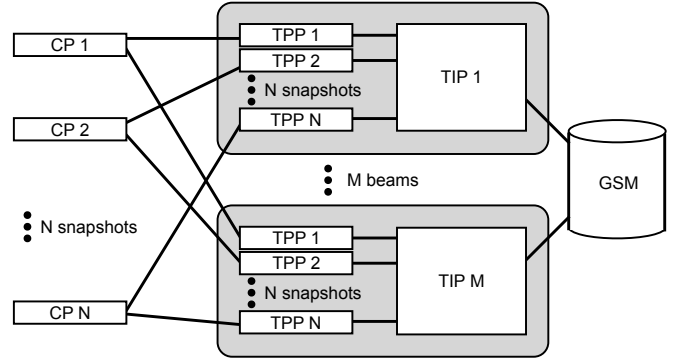


Fig. 6. The scheme for calibrating, processing, and combining individual snapshots of an MSSS field. Each field is observed in N snapshots, and each snapshot observation simultaneously observes M beam directions. In the case of MSSS-LBA, $N = 9$, and M is either 2 or 5 depending on whether the observations are done in 16-bit or 8-bit mode. For MSSS-HBA, $N = 2$ and $M = 3$ or 6. CP stands for Calibrator Pipeline; TPP for Target Pre-processing Pipeline; TIP for Target Imaging Pipeline; and GSM for Global Sky Model. See Figure 5 for an overview of how these pieces fit together in more detail, and for the steps that make up each segment of the full pipeline.

3. Calibration and imaging strategy

The MSSS commissioning project has driven the development of the first version of the standard imaging pipeline (SIP; Heald et al. 2010), which can be scheduled by the control system to run automatically on the central processing cluster upon completion of the individual observations. The SIP embodies the calibration strategy described in this section, and is now being upgraded to allow improved image quality at higher angular resolution.

We illustrate the processing chain followed by a single observation in Figure 5. The somewhat more complicated survey organization in Figure 6 shows a schematic view of the overall processing pipeline, which combines multiple snapshots and calibration observations to create final combined images and feed source catalogs into the LOFAR Global Sky Model (GSM)

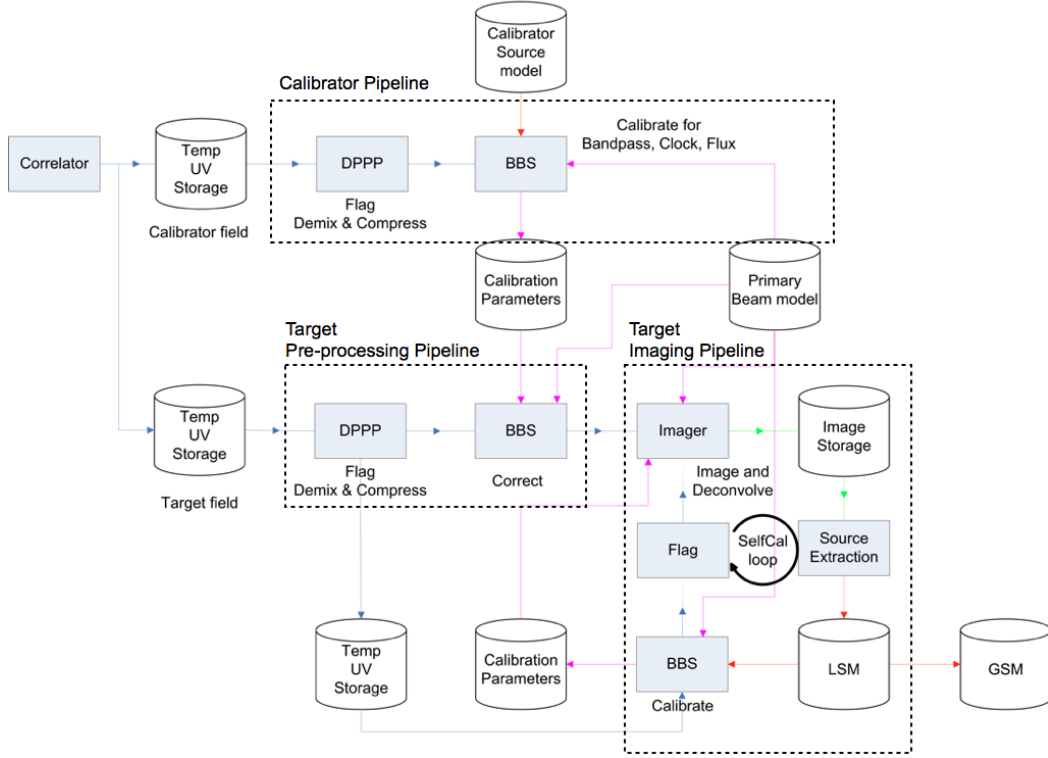


Fig. 5. Sketch of the MSSS calibration and imaging pipeline. See the text for a description.

database. In these diagrams, cylinders indicate data products, and blocks indicate programs and pipeline segments. The full pipeline is broken up into three main components. The first is the Calibrator Pipeline (CP), which applies some pre-processing steps that are described below to the calibrator scans, and performs primary calibration using a known and well-understood calibrator model. The Target Pre-processing Pipeline (TPP) performs the same pre-processing steps as in CP, and subsequently uses the station gains derived in CP to apply the primary calibration to the individual field snapshots. The resulting calibrated snapshots are stored until all snapshots of a particular field are completed, after which the Target Imaging Pipeline (TIP) begins. This final stage is the heart of the pipeline, and consists of imaging the field and optionally running a self-calibration cycle which is still in need of further development. We now proceed to detail the various pieces of the pipeline.

3.1. Pre-processing steps

Flagging for RFI is performed in a standard and automatic fashion using the AOFlogger (Offringa et al. 2010). This program has been shown to provide excellent RFI excision with minimal false positives. Details of the typical performance of the implemented algorithm on LOFAR data, along with representative RFI statistics, are presented by Offringa et al. (2013).

Following the flagging step, the demixing technique (van der Tol et al. 2007) is applied in order to remove far off-axis, bright sources (primarily the so-called “A-team”: Cygnus A, Cassiopeia A, Virgo A, and Taurus A) from the visibility data. The automatic pipeline calculates the distance to the A-team sources from the target (and calibrator) fields. Sources within distance ranges determined empirically from commissioning experience are selected for demixing.

Compression of the data to a manageable volume is done automatically following the demixing step. Typically, in both LBA and HBA the data volume is reduced by a factor of 10 after averaging and calibration have been performed. The compression factors were selected to minimize bandwidth and time smearing effects, as well as retain sufficient time resolution to allow capturing time variable ionospheric effects. In this way we are able to restrict our estimates of position-dependent survey sensitivity to only consider the combination of station beam pattern and survey pointing grid.

3.1.1. Bandwidth smearing

The effect of finite bandwidth is to partially decorrelate the signal and leads to a radial smearing of sources far from the phase tracking center. Assuming a square bandpass and a synthesized beam with a Gaussian profile, the magnitude of the flux loss can be approximated as given by Bridle & Schwab (1999):

$$\frac{I}{I_0} = \frac{\sqrt{\pi}}{2\sqrt{\ln 2}} \frac{\theta v_c}{r \Delta \nu} \operatorname{erf} \left(\sqrt{\ln 2} \frac{r \Delta \nu}{\theta v_c} \right) \quad (3)$$

where θ is the synthesized beam size (FWHM), v_c is the central frequency of the observation, r is the distance from the phase center, and $\Delta \nu$ is the bandwidth.

For LOFAR, the individual subband width (using the standard 200 MHz clock) is 195.3125 kHz and in MSSS observations is divided into 64 channels. For a characteristic angular resolution of $2'$, we have calculated smearing factors for each of the MSSS band frequencies, and a field radius corresponding to half of the station beam HPBW (see § 2.1 and 2.2). The resulting bandwidth smearing curves have been calculated for different frequency averaging parameters and are displayed in Figure 7. Clearly in the case of the LBA survey, at least 8 channels per

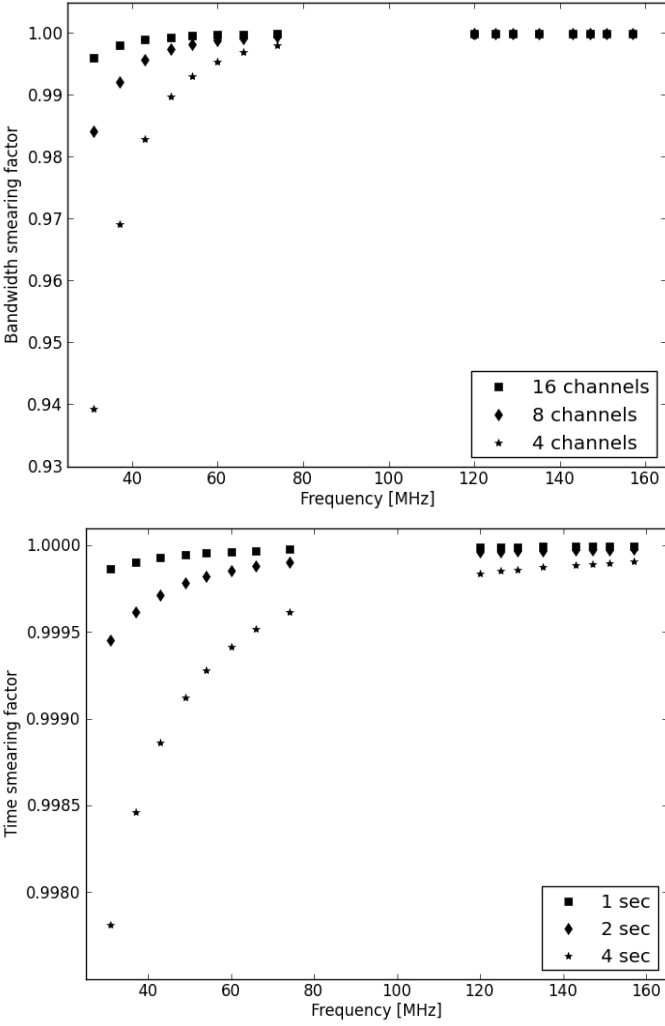


Fig. 7. Bandwidth (*top*) and time (*bottom*) smearing factors relevant to LOFAR MSSS observations, expressed as percentages and where unity is equivalent to no smearing. These values are calculated for $2'$ angular resolution and for sources at the half-power point of the station beam. In the top panel, points are plotted for averaging single subbands to 4 (*stars*), 8 (*diamonds*), and 16 (*squares*) channels. In the bottom panel, the smearing is calculated for visibility time averaging intervals of 1 (*squares*), 2 (*diamonds*), and 4 (*stars*) seconds.

subband must be retained in order to keep the effect of smearing to $\lesssim 1 - 2\%$. For the HBA portion, the frequency averaging does not play such a crucial role.

We thus retain 8 channels per subband in LBA for a maximum allowable bandwidth smearing factor at the lowest frequencies. In HBA, we retain 4 channels per subband to allow re-processing at higher angular resolution without unacceptable smearing losses. Note that in the LBA, re-processing the data in order to image at higher resolution will require either redoing the pre-processing steps with a lower frequency averaging factor, or acceptance of a substantial smearing factor at the lowest frequencies.

3.1.2. Temporal resolution

Another effect that needs to be accounted for is time-average smearing. Again referring to the expressions given by Bridle & Schwab (1999), we assess the impact on MSSS data using:

$$\frac{I}{I_0} = 1 - 1.22 \times 10^{-9} \left(\frac{r}{\theta}\right)^2 \tau_a^2 \quad (4)$$

where τ_a is the averaging time. The estimated time smearing factors are shown in Figure 7.

The effect of time smearing is considerably less than the impact of bandwidth smearing. For small time averaging intervals, the effect is negligible. The smearing is also less important than the need to retain high time resolution for recovery of ionospheric phase disturbances during the calibration process. We average the time steps to 2 seconds in order to recover high-quality station gain phases. This is illustrated in § 3.4.

3.2. Primary and secondary calibration

The primary calibrators for MSSS are listed in Table 2, and are based on the calibration model presented by Scaife & Heald (2012). These sources are mostly chosen to be compact on Dutch baselines (approximately 80 km or less), bright enough to give sufficient signal-to-noise per visibility, and have well-characterized radio spectra. The exception is Cygnus A, which is used as a primary calibrator in the LBA portion of MSSS, despite being a very complicated extended source. It does however have a very well determined source model, based on extensive commissioning work (summarized by McKean et al. 2011; McKean 2015).

Observational verification of these primary calibrator sources started early in the MSSS test program, and revealed that while the brightest sources in the low band (3C196, 3C295, and CygA) were suitable primary calibrators, the others were too weak and/or too close to A-team sources to provide stable gain amplitude solutions. These fainter sources are still useful for the HBA portion of the survey but are not utilized in the LBA portion.

Primary (flux) calibration is handled with two different strategies in the LBA and HBA parts of the survey. In the LBA part, we take advantage of the fact that the individual dipoles are sensitive to emission from the entire visible sky, and observe with a simultaneous calibrator beam. The calibrator at the highest elevation is used, regardless of the distance between calibrator and target fields. The calibrator beam uses the exact same frequency coverage as the target fields and runs for the full length (11 minutes) of the target snapshots. This ensures sufficient time samples to obtain a stable gain amplitude solution. The CP obtains, and then exports, the median gain amplitude solution per station (along with the corresponding gain phase which is not actually used) from the calibrator beam, for application to the flagged and demixed target data in the TPP. On the other hand, a different strategy is used for the HBA observations. The analog HBA tile beam limits the field of view to typically 23 degrees HPBW at 150 MHz. This means that a bright, compact calibrator is not always available within the field of view near the targets. Therefore, the calibrator is observed alone (before the target snapshot) for 1 minute. Because the instantaneous sensitivity of the HBA system is much higher than that of the LBA system, stable gain amplitudes are obtained with a much shorter observing interval. As with LBA, the HBA calibrator beam covers the same frequencies as the target beams, and the CP exports

Table 2. Primary MSSS calibrator sources

Source ID	RA (J2000.0)	Dec (J2000.0)	$S_{150\text{MHz}}$ (Jy)	Spectral index	Morphology	LBA calibrator
3C48	01h37m41.3s	+33d09m35s	64.768	(-0.387,-0.420,0.181)	point	No
3C147	05h42m36.1s	+49d51m07s	66.738	(-0.022,-1.012,0.549)	point	No
3C196	08h13m36.0s	+48d13m03s	83.084	(-0.699,-0.110)	double	Yes
3C286	13h31m08.3s	+30d30m33s	27.477	(-0.158,0.032,-0.180)	point	No
3C295	14h11m20.5s	+52d12m10s	97.763	(-0.582,-0.298,0.583,-0.363)	double	Yes
3C380	18h29m31.8s	+48d44m46s	77.352	(-0.767)	point+diffuse	No
CygA	19h59m28.3s	+40d44m02s	10690.0	(-0.670,-0.240,0.021)	FRII	Yes

the median gain amplitude per station. These are subsequently applied to the target snapshot data in the TPP.

Following the application of the primary flux calibration, the station phases remain uncalibrated (in the direction of the target field). The phase calibration takes place in the Target Imaging Pipeline, described in § 3.4.

3.3. Automatic data quality filtering

Much of the MSSS-LBA data were obtained early in LOFAR’s lifetime, and this meant that much of the data were taken in unstable conditions. It turned out that typical observations included one or more bad stations (because of bad digital beam forming, network connection issues, or other reasons). We therefore incorporated conservative filtering steps into the pipeline, to identify and flag stations performing well outside of the normal bounds. The most important step considers the statistics of each station, and flags those that have an exceptionally large number of baselines with high measured noise. Before LOFAR’s digital beams were well controlled, this step primarily removed stations with poorly focused beam response.

3.4. Target Imaging Pipeline

The TIP stage of the MSSS pipeline combines the flagged, demixed, and flux-calibrated target snapshot observations to generate an initial image of the field. The TIP also optionally performs a self-calibration major cycle. Because it is decoupled from the pre-processing part of the pipeline, it can be run in an asynchronous manner with respect to the observational part of MSSS.

As a first step, the individual 2-MHz band snapshots are combined, resulting in 8 visibility data sets per LBA or HBA field. These bands are treated separately throughout the TIP. The phase-only, direction-independent calibration is done using a VLSS-based sky model but taking the station sensitivity patterns into account. Example gain phases are shown in Figure 8. The phases are shown for two representative stations, CS302 (about 2 km southwest of the central group of six stations, collectively called the “superterp”) and RS306 (about 15 km west of the superterp). These are shown as a function of time, with one set of phases for each of the 8 frequency bands and displayed here with an arbitrary offset for visual clarity. Phase calibration is performed such that an independent solution is produced for each 2 second timestep.

3.4.1. Imaging MSSS data

Imaging MSSS data is performed with the LOFAR imager, called the *awimager* (Tasse et al. 2013). It is based on the CASA imager including *w*-projection (Cornwell et al. 2008), and also includes a LOFAR-specific implementation of A-projection

(Bhatnagar et al. 2008) that treats the dipole and station response as time- and direction-dependent, full polarization terms in the measurement equation (e.g., Hamaker et al. 1996) during imaging and deconvolution.

Our implementation of the LOFAR beam includes three layers. First, the LOFAR element beam is modelled through a full EM simulation (not including mutual coupling) and implemented in our software as a polynomial fit in elevation, azimuth, and frequency. The HBA analog tile beam is also included as the DFT of the dipole positions within a tile, and rotated to account for the orientation of each station (as described by van Haarlem et al. 2013, each HBA station is rotated to reduce the sensitivity to bright far off-axis sources). Finally, the digital station beam for both LBA and HBA is calculated using a direct Fourier transform (DFT) of the dipole (LBA) or tile (HBA) positions in each individual station. Missing dipoles (LBA) and tiles (HBA) are indicated as such in the visibility data sets recorded by the correlator, and left out of the beam prediction during calculation. For MSSS data, the beam is applied in the *awimager* such that it is considered to be constant within frequency blocks of width 100 kHz, and time blocks of 5 min.

Our initial imaging run per field incorporates projected baselines shorter than $2\text{ k}\lambda$. For fields at declination $\delta \leq 35^\circ$, we leave out baselines shorter than 100λ . This imaging run is performed with a simple, shallow deconvolution strategy (using 2500 CLEAN iterations). After re-calibrating the data on the basis of this first imaging round (see § 3.4.3), we update the imaging parameters in preparation for final catalog creation: the maximum baseline length is increased to $3\text{ k}\lambda$. After an initial shallow deconvolution, we create a mask on the basis of a source detection round performed in the way described in § 3.4.2, and subsequently perform a deep deconvolution using the mask to limit the locations of CLEAN components. The final deconvolution is limited by reaching a cutoff of 0.5σ instead of by limiting the number of components. All imaging steps use Briggs weighting (Briggs 1995) with a robust parameter of 0.

A unique benefit of incorporating a time-, frequency-, and direction-dependent term in the imaging and deconvolution step through the A-projection algorithm is the ability to directly incorporate ionospheric corrections. We implement this procedure for our LBA data, as described in § 3.4.3. For the application of the ionospheric correction we increase the time resolution to 10 sec in order to capture the rapidly variable phases.

3.4.2. Source finding

The source finding is performed using two complementary source extraction softwares: PyBDSM³ and PySE⁴.

Both packages allow calculation of rms and mean images and identification of sources in radio maps through the use ei-

³ <http://tinyurl.com/PyBDSM-doc>

⁴ <http://docs.transientskyp.org/tkp/master/tools/pyse.html>

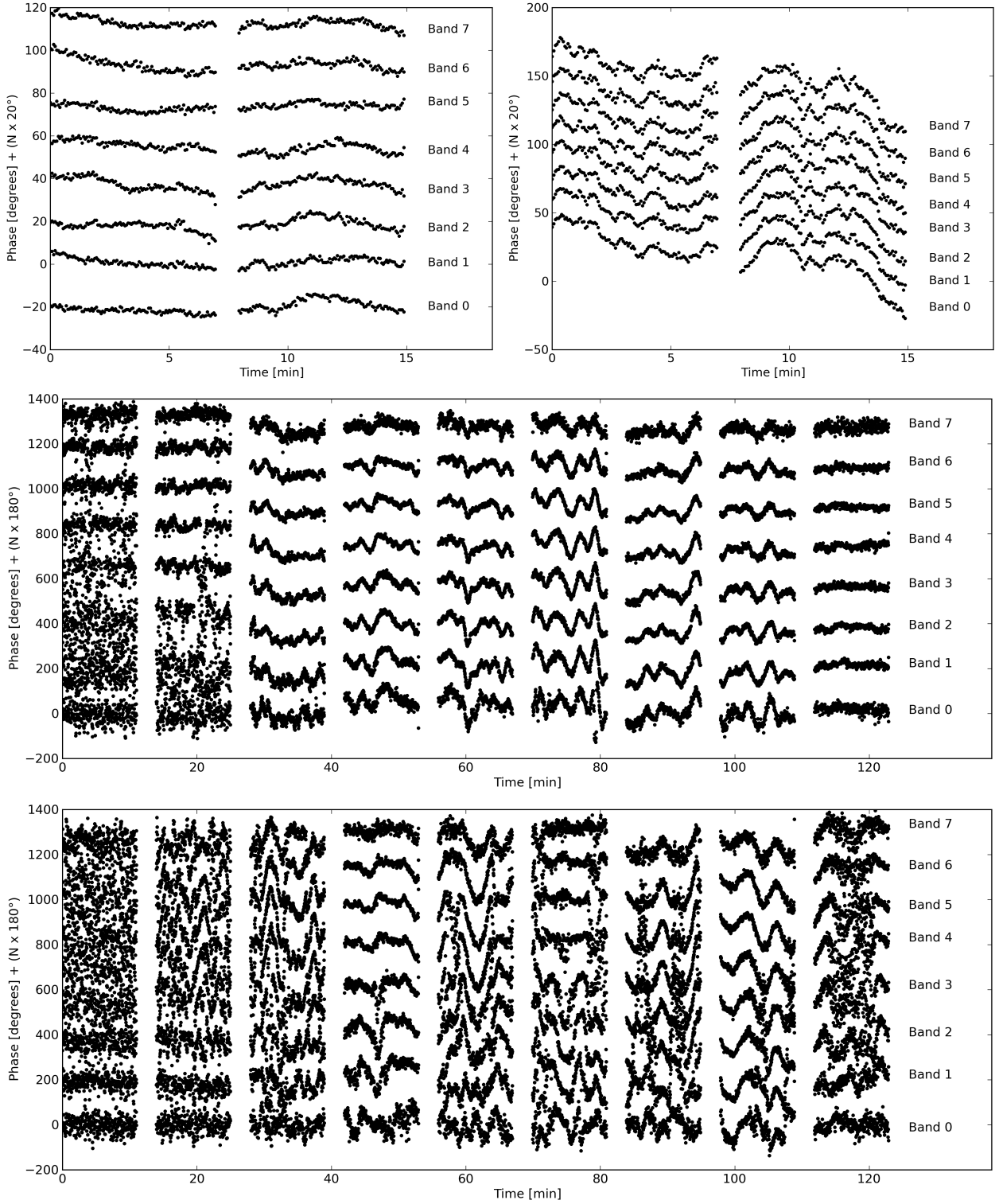


Fig. 8. Gain phases for HBA (*top row of panels*) and LBA (*bottom two panels*), referenced to CS002HBA0 and CS002LBA respectively. (CS002 is one of the six superterp stations.) The phases are shifted vertically for display purposes. They correspond to the (0,0) element of the station gain matrix for CS302 (*top left and middle*) and RS306 (*top right and bottom*). The gaps between snapshots are compressed for display purposes, and correspond to 4 hours for HBA and 45 minutes for LBA. These are the gain phases determined for the HBA and LBA fields H229+70 and L227+69 (see Table 3).

ther of a False Detection Rate (FDR) method (Hopkins et al. 2002), or of a threshold technique that locates islands of emission above some multiple of the noise in the image. Gaussians are then fitted to each island for accurate measurement of source properties. Both PyBDSM and PySE allow to use separate detec-

tion and analysis image files for island definition and Gaussian fitting respectively.

While PySE has been designed as source finding tool devoted to the LOFAR Transients Key Project and it is therefore conceived for the detection of unresolved sources, PyBDSM has

been programmed for the more general search of both compact and diffuse sources. PyBDSM thus allows fitting of multiple Gaussians to each island or grouping of nearby Gaussians within an island into sources. In addition a PyBDSM module is available to decompose the residual image resulting from the normal fitting of Gaussians into wavelet images of various scales. This step is useful for automatic detection of diffuse sources. In the following, we therefore combine PyBDSM and PySE results only in the case of point-like sources. Our source finding strategy consists of running both PyBDSM and PySE separately and then combining the results. Eight different joint PyBDSM/PySE catalogs are therefore initially produced for each of the 8-band maps in both HBA and LBA, and these are subsequently merged to give the final multi-frequency catalog.

We define an island threshold to determine the region within which source fitting is done and an additional limit parameter in such a way that only islands with peaks above this absolute threshold will be used. For MSSS images, we set these two thresholds to 5σ and 7σ , respectively. In addition, similarly to what is extensively done in the visible domain (see e.g. Szalay et al. 1999), we use an 8-band combined image (see below for a description) and each single band map as detection and analysis images respectively. The use of a combined map for island definition optimizes sensitivity to faint sources. Since all detections are undertaken using a single image, in addition, this procedure alleviates the task of matching the 8-band catalogs.

The 8-band images on which we run the source finder tools are produced using the same uv -range and convolved to a common resolution using the MIRIAD (Sault et al. 1995) task CONVOL. We do this both for primary-beam (PB) and non-primary-beam (NPB) corrected maps. These latter are used to produce the combined map, obtained by performing an inverse-variance weighted average of the 8-band NPB corrected maps (i.e., the weight per image is $w_i = 1/\sigma_i^2$ where σ_i is the rms of image i). This combined map is used as the detection image, while the individual 8-band PB corrected maps are used as analysis images. In such a way, we avoid fake detections in the image borders (which may be caused by the increase of the rms related to PB correction), while obtaining properly corrected fluxes per source as the output of the source finders.

For the combined catalog description and additional detailed information regarding the method by which it is produced, see § 4.2.

3.4.3. Calibration stability and ionospheric corrections

To produce the final survey output, we run the TIP twice. The first time incorporates the VLSS-based sky model as described in § 3.4. For the second pass, we repeat the phase calibration using a sky model created from the first-pass calibration and imaging round. On the basis of this new phase calibration, we generate a new set of images (as described in § 3.4.1) and source catalogs. The intention of this step is to minimize the effect of any spurious sources that may be present in the initial sky model and to ensure that the MSSS catalog is based on an internally consistent calibration cycle. This procedure has been followed for the representative data set considered in § 5.

For the low frequency and large field of view intrinsic to LOFAR observations in the LBA band, ionospheric effects are strong even when imaging at the modest $\approx 2'$ resolution utilized for MSSS. The clearest effect in the image plane is the presence of spiky artefacts around the brightest sources. To deal with this we have implemented a scheme similar to the Source Peeling and Atmospheric Modeling (SPAM; Intema et al. 2009)

approach that has been successfully used for VLA and GMRT data. We briefly summarize the procedure here; a full description will be provided in a forthcoming publication. The sky model is divided into approximately 30 source groups, and each group is used to derive a phase solution at each frequency. These 30 source groups cover the entire field of view visible at 30 MHz; to trace the frequency behavior of the calibration phases in those directions at the highest frequencies, where the field of view is much smaller, we utilize simultaneously observed flanking beams. Thus ionospheric phases are only available across the full field of view for the central field in a multiplexed observation like MSSS. For the dataset considered in § 5, only the central field (L227+69) can be processed in this manner.

The frequency dependent phases include two terms: a non-dispersive clock delay term⁵ and a dispersive ionospheric delay term. The clock term is constant in all directions at a given time, while the dispersive term is direction-dependent. To isolate the ionospheric term we subtract the phases determined in one direction from those in all other directions, leaving a differential ionospheric phase term per direction and per station. By considering the phase of each station in each direction as a single ‘‘pierce point’’ through a single thin-layer ionosphere, these values are used to fit a ‘‘screen’’ of ionospheric total electron content (TEC) at a particular height. The difference between data and fitted screen is used to identify an optimized TEC screen height, typically around 100 – 200 km. The TEC screen can be used as an input to the `awimager` to correct the phase distortions across the field of view, as a function of both frequency and time.

4. Standard data products

The primary output of MSSS is a catalog containing positions and flux densities for all confidently detected sources, as well as extents and orientations for resolved sources. Spectral behavior of the sources is also provided. The MSSS catalog is stored in the LOFAR GSM database, implemented in a fully VO-compliant system based on the Data Center Helper Suite (DaCHS; Demleitner 2014).

Processed visibilities will be stored in the LOFAR long term archive (LTA) for future re-processing, for use by science groups that wish to reprocess the data to search for, e.g., polarization or to perform long-baseline imaging (see § 6). In addition, raw visibilities are always stored in the LTA immediately after observation. At the conclusion of the TIP, the images are imported to a postage-stamp server⁶ which allows inspection of images with catalog overlays and multi-frequency source spectrum pop-up plots, as well as providing direct-download links to FITS files.

Following verification of the survey results, the survey output (images and catalogs) will become fully public.

4.1. MSSS Images

The MSSS image products will be released in FITS format, and will consist of mosaics corresponding to the fields specified in § 2.4. Each mosaic consists of sixteen 2 MHz bandwidth images at the central frequencies listed in Table 1, and two 16 MHz full bandwidth images, one for LBA and the other for HBA.

⁵ LOFAR stations only share a single clock within the core area; the remote stations are on independent clocks.

⁶ <http://msss.astron.nl>

4.2. MSSS Catalog

The MSSS catalog is generated in several steps. First, the PySE and PyBDSM source finders are run on all individual frequency bands using the combined maps as detection images (see Section 3.4.2 for details). For each source finder, the detected sources are then associated across the individual frequency bands in order to generate a concatenated multi-frequency source catalog. The association is performed by calculating the angular distance between sources in any pair of individual frequency band catalogs. A match is determined to be positive if each element of the pair is mutually the nearest to its counterpart from the other catalog. This criterion ensures that sources have exclusive pairing, as opposed to possible multiple associations. An additional threshold rule is also used in order to reject sources that are too distant and might be spurious association; hence we require distance $\leq 3\sqrt{\sigma_1^2 + \sigma_2^2}$, where $\sigma_{1,2}$ are the positional uncertainties in the first and second catalog, respectively. We chose a threshold of 3σ after verifying that the curve of growth of positive matches started plateauing around this level. After the source association is completed, we calculate the final position of each source – RA and Dec separately – as the average position among the frequency bands in which it was detected weighted by the positional uncertainties. The final positional errors are calculated by propagating the errors accordingly.

Following the source association within the PySE and the PyBDSM catalogs, sources detected with each source finder are also associated in order to generate the final catalog. The same pairing process as explained above is used for this step. However, in order to preserve consistency in the final catalog, we did not attempt to calculate average values for the various reported fields. Rather, we chose the PyBDSM fields to prevail over those from PySE when both values existed. Hence, the reported IDs and positions are taken from PyBDSM unless a source was only detected by PySE. Similarly, for a given frequency band, the reported flux properties are those found by PyBDSM unless the source was only detected in this particular frequency band by PySE. Each frequency band possesses a field `SFFLAG nnn` that indicates which, if not none or both, source finder the source was detected with at frequency nnn MHz. By considering the results from both source finders together in this way, we can add confidence to the reality of individual detections; thus we recommend using sources detected by only one source finder with caution.

Finally, we perform a post-concatenation analysis in order to determine the spectral properties for each source. For this step, only the PyBDSM fluxes are used – again this is done in order to ensure consistency since the flux scale between the two source finders may suffer from biases. The spectrum of each source is fitted with the functional form (see also Scaife & Heald 2012):

$$S = A_0 10^{A_1 \log(\nu/150 \text{ MHz}) + A_2 \log^2(\nu/150 \text{ MHz})}. \quad (5)$$

Given the large number of sources to be fitted and the fact that the posterior distribution of the spectral fit should be well-behaved – this is a linear least-square fit to a polynomial in $\log S$ space – we use a Levenberg-Marquardt χ^2 minimisation algorithm to determine the best-fit parameters and errors. The curvature term (A_2) is only fitted for sources displaying sufficient evidence for the higher-order term, which is assessed using the corrected Akaike information criterion (Burnham & Anderson 2002): $AIC_c = \chi^2 + 2k + \frac{2k(k+1)}{n-k-1}$, where k is the number of fit parameters and n is the number of data points. The model (with or

without the curvature term) with the lowest AIC_c value should prevail.

We use a locally determined effective beamsize to deconvolve the source sizes reported by PyBDSM, and classify sources as extended if the deconvolved size is nonzero.

The MSSS catalog has the following columns. First, a set of parameters that are common for both the point source catalog and extended source catalog:

ID	Source ID, formed as <i>Jhhmms + ddmmss</i> using the IAU convention.
RA	Source J2000 Right Ascension, in decimal degrees.
DEC	Source J2000 Declination, in decimal degrees.
e_RA	Error on source J2000 Right Ascension, in seconds of time.
e_DEC	Error on source J2000 Declination, in arcseconds.
SFFLAG nnn	Flag indicating which source finder was the source identified with at nnn MHz (0 means it was detected in both; 1 means it was detected only in PyBDSM; 2 means only in PYSE; 3 means none). Note that if the source was identified by both source finders, the reported flux values are those of PyBDSM.
Sint nnn	Source integrated flux at nnn MHz, in Jy.
e_Sint nnn	Error on source integrated flux at nnn MHz, in Jy.
Spk nnn	Source peak flux at nnn MHz, in Jy.
e_Spk nnn	Error on source peak flux at nnn MHz, in Jy.
A0	Spectral flux at 150 MHz, A0 in Equation 5.
e_A1	Error on spectral spectral flux at 150 MHz.
A1	Spectral index, A1 in Equation 5.
e_A1	Error on spectral index.
A2	Spectral curvature, A2 in Equation 5.
e_A2	Error on spectral curvature.
NDET	Number of bands in which the source was detected.
NDET_LBA	Number of LBA bands in which the source was detected.
NDET_HBA	Number of HBA bands in which the source was detected.
NUNRES	Number of bands in which the source is unresolved.
NUNRES_LBA	Number of LBA bands in which the source is unresolved.
NUNRES_HBA	Number of HBA bands in which the source is unresolved.
MOS_ID	Mosaic name from which the source was extracted.
CAL_ID	Primary flux calibrator(s) used to set the flux scale in the vicinity of the source.

A set of parameters that are only included for the extended source catalog:

MAJAX nnn	Major axis of fitted ellipse at nnn MHz, in decimal degrees.
MINAX nnn	Minor axis of fitted ellipse at nnn MHz, in decimal degrees.
PA nnn	Position angle of fitted ellipse at nnn MHz, in decimal degrees.
e_MAJAX nnn	Error on major axis, in decimal degrees.
e_MINAX nnn	Error on minor axis, in decimal degrees.
e_PA nnn	Error on position angle, in decimal degrees.

This catalog has 99 columns for the point sources, and $99 + 96 = 195$ columns for extended sources. Assuming that there will be 10^5 sources (see § 5) with about 5% of those extended, then that will lead to about 10.4 million catalog entries.

5. Initial MSSS imaging results

MSSS observations are typically performed for several hours per week within the rest of the LOFAR schedule. The HBA segment has been fully observed and initial images have been created. While the survey calibration processing is still ongoing, we highlight a representative portion of the sky to illustrate the output that will be forthcoming for the full northern sky. For this we select a 100 square degree patch of sky that has been used repeatedly to test imaging pipeline performance. The field was randomly selected and we refer to it here as the MSSS Verification Field (MVF). It includes a few moderately bright point-like sources but no bright, complicated 3C or 4C sources and is otherwise distant from the troublesome A-team sources. The Galactic contribution to the sky brightness is relatively unimportant in this direction (Galactic coordinates ($l = 108^\circ, b = 44^\circ$) at the center of the MVF).

The mosaics in this region are created from 9 LBA fields and 32 HBA fields, as illustrated in Figure 9. These fields were not all observed at the same time or even on the same day. The observing summary is listed in Table 3. The primary flux calibrator for fields H244+70 and H245+75 was 3C380, and the primary flux calibrator for all other fields was 3C295. After convolution to a common beam size, the effective resolution in HBA is $108''$, and in LBA $166''$. Images of the frequency-averaged LBA field, and HBA mosaic, are shown in Figures 10 and 11, respectively.

Due to the ionospheric processing scheme described in § 3.4.3, only the central LBA field (L227+69) is used to generate the LBA part of the MVF catalog. Moreover, only 7 of the 9 LBA snapshots were used due to particularly bad ionospheric quality during the first 2 snapshots (see Figure 8). The HBA portion of the catalog was produced based on the combination of all fields listed in Table 3. All told, 1234 unique sources were identified within the 100 square degrees of the MVF (307 in LBA, 1234 in HBA). A simple projection to the full MSSS survey area would suggest approximately 250,000 sources, but taking into account reduced sensitivity at low declination and Galactic latitude, as well as poor image quality near extremely bright sources, we expect to recover between 150,000 – 200,000 sources in the full MSSS catalog.

We present the spectral index distribution determined on the basis of the MVF catalog in Fig. 12. We consider all sources with a cataloged A_0 value greater than 200 mJy (634 out of 1234 sources). Considering the spectral index determined using all cataloged frequencies (recorded in column A1), the mean and median values are -0.57 and -0.64 , respectively. These are somewhat more shallow than spectral indices determined for the same sources from HBA fluxes alone (mean and median of -0.81 and -0.82 , respectively). Part of this may be due to spectral turnovers at LBA frequencies, although some is likely due to measurement errors. We note that the HBA-only spectral indices have a systematic error due to beam effects not incorporated in the beam model described in § 3.4.1. The error is estimated at the level of 0.05 ± 0.22 for the MVF region on the basis of more recent electromagnetic simulations of the HBA stations including the effects of mutual coupling. Because these simulations are still under development, and the correction at the high elevation of the MVF snapshots is expected to be very small, we have not adjusted the HBA spectral indices presented in the bottom panel

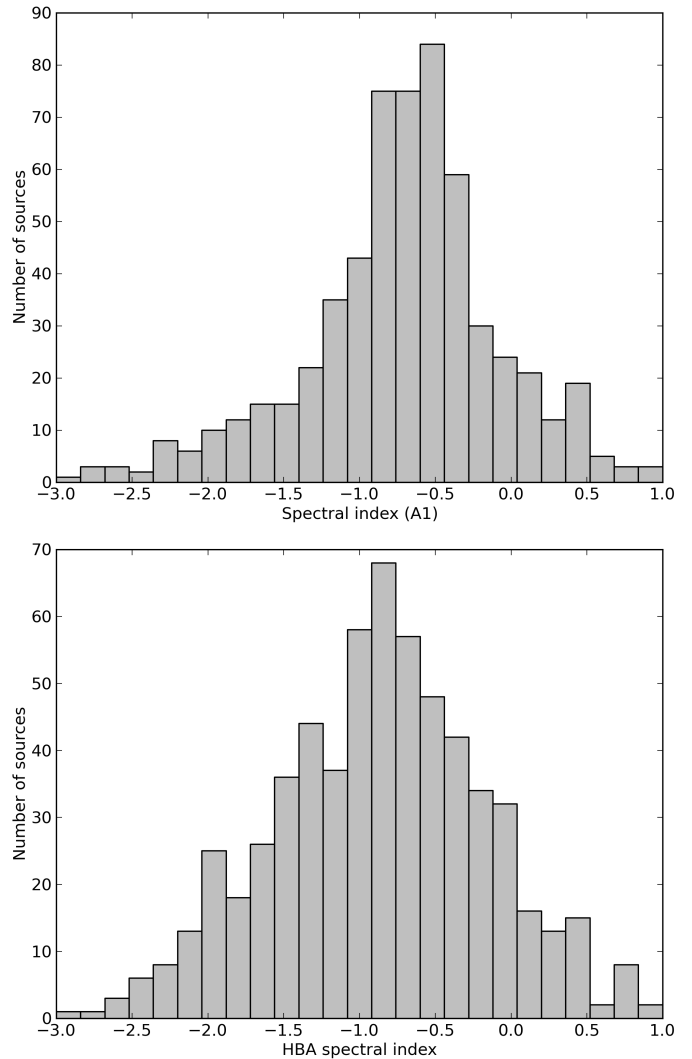


Fig. 12. Spectral index histograms for the MVF catalog sources with $A_0 > 0.2$, based on the cataloged A1 values (*top*), and the HBA values only (*bottom*).

of Fig. 12. We will fully address this issue during the creation of the full MSSS catalog.

5.1. Completeness

We determined the completeness of the MVF portion of the survey in the standard way through the use of Monte Carlo simulations, injecting simulated sources into residual images from the survey and attempting to recover them with the source finder. We used PyBDSM for this process; results with PySE would be expected to be very similar. The only complication arises from the fact that averaged images (from all LBA and HBA bands) are used as detection images in the cataloging process. Therefore, in addition to finding the completeness in individual bands, we replicated the process used in cataloging to generate and apply detection images.

In detail, we generated residual maps from the actual images used for the cataloging, having first removed any detected sources with PyBDSM: this ensures that the noise and its spatial distribution are consistent with that of the real data. We drew simulated sources from a power-law flux density distribution with $\frac{dN}{dS} \propto S^{-1.6}$, with fixed upper and lower flux densities cho-

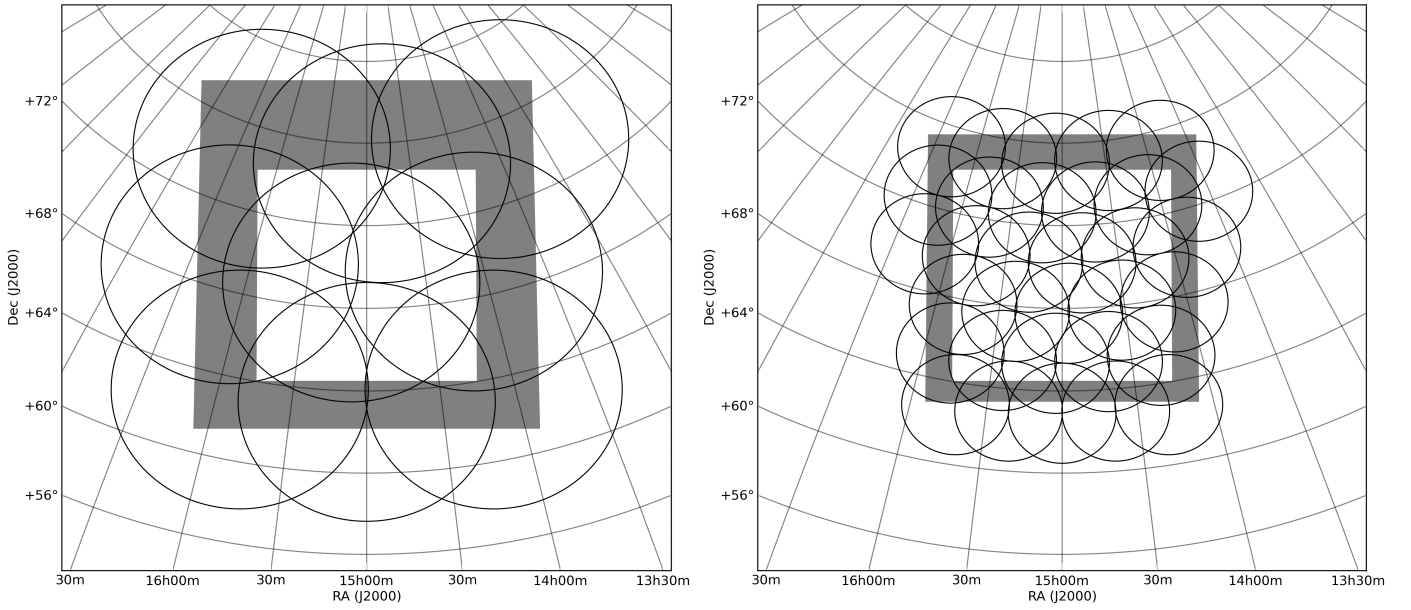


Fig. 9. Mosaic layout of the MSSS Verification Field (MVF). *Left:* The nine LBA fields making up the MVF, overlaid on the $10^\circ \times 10^\circ$ mosaic field (central white square). The gray border around the mosaic area is a guard area used to ensure that sufficient edge fields are included and to ensure flat sensitivity within the mosaic. *Right:* The 32 HBA fields making up the MVF, overlaid on the same central mosaic field. The guard border is smaller in proportion to the HBA field diameter.

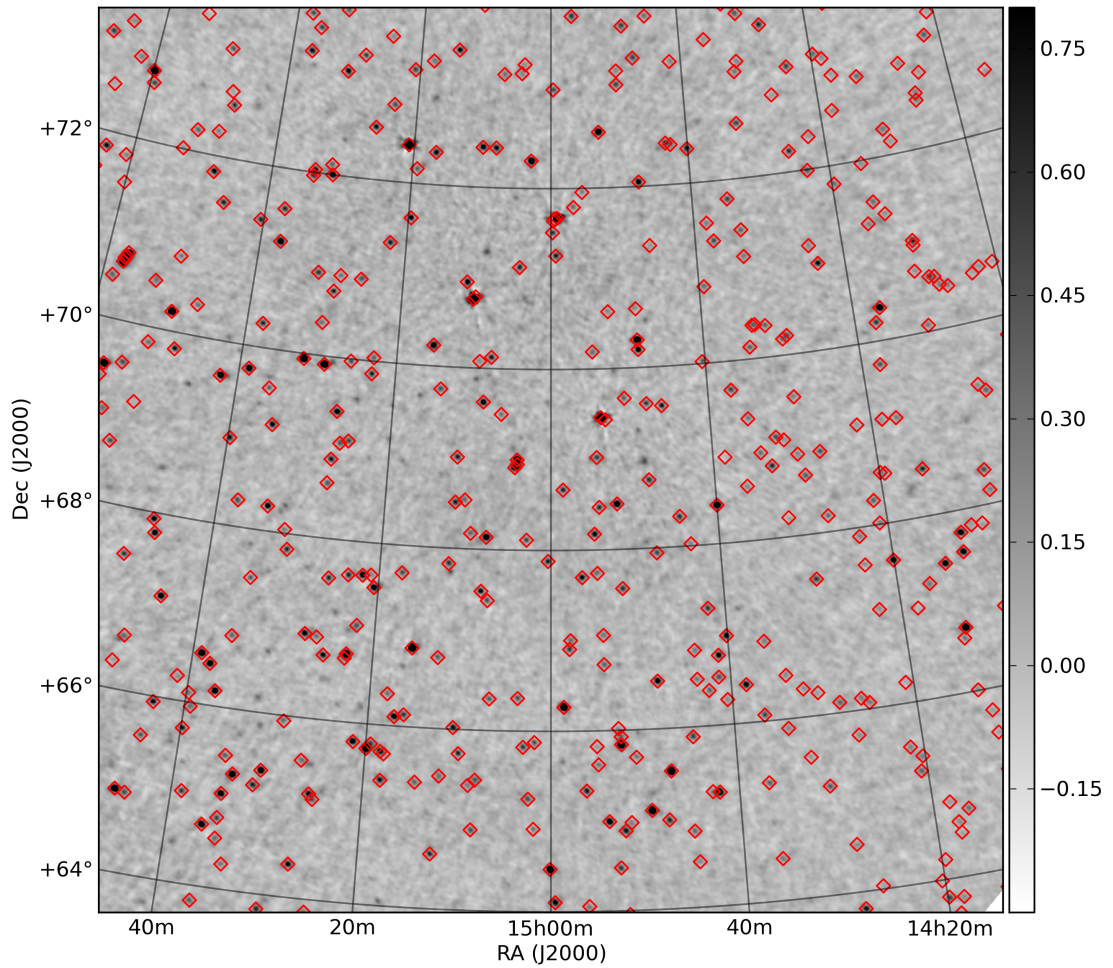


Fig. 10. LBA full-bandwidth central field of the MVF, after ionospheric correction and displayed here without primary beam correction for clarity. The noise level is 39 mJy beam^{-1} , and the synthesized beam is $166''$. The colorbar units are Jy beam^{-1} . Diamonds mark the positions of cataloged VLSSr sources.

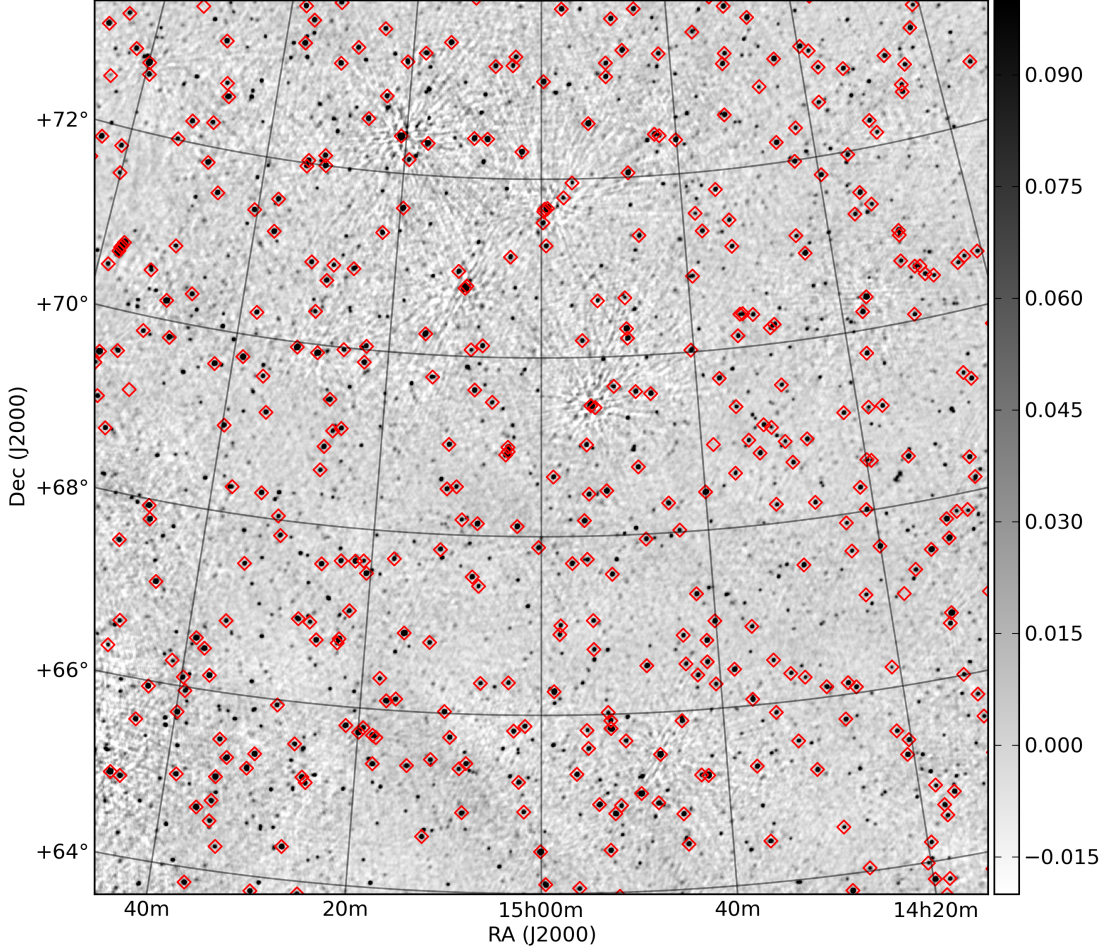


Fig. 11. HBA full-bandwidth mosaic of the MVF, displayed here without primary beam correction for clarity. The noise level is 5 mJy beam^{-1} , and the synthesized beam is $108''$. The colorbar units are Jy beam^{-1} . Diamonds mark the positions of cataloged VLSSr sources.

Table 3. MSSS Verification Field Observing Log

Field	Date								
L212+63	2013 Apr 8	H214+63	2013 Apr 21	H231+65	2013 Apr 21	H215+70	2013 Apr 21	H228+73	2013 Feb 15
L225+63	2013 Mar 18	H220+63	2013 Apr 21	H237+65	2013 Apr 21	H222+70	2013 Feb 15	H236+73	2013 Feb 15
L238+63	2013 Apr 8	H225+63	2013 Apr 21	H212+68	2013 Apr 21	H229+70	2013 Feb 15	H244+73	2013 Apr 21
L211+69	2013 Mar 18	H230+63	2013 Apr 21	H218+68	2013 Feb 15	H236+70	2013 Feb 15	H208+75	2013 Apr 21
L227+69	2013 Mar 18	H236+63	2013 Apr 21	H224+68	2013 Feb 15	H244+70	2013 Feb 22	H217+75	2013 Apr 21
L243+69	2013 Mar 18	H214+65	2013 Apr 21	H231+68	2013 Feb 15	H204+73	2013 Apr 21	H226+75	2013 Apr 21
L201+75	2013 Apr 8	H220+65	2013 Feb 15	H237+68	2013 Feb 15	H212+73	2013 Apr 21	H235+75	2013 Apr 21
L222+75	2013 Mar 18	H226+65	2013 Feb 15	H208+70	2013 Apr 21	H220+73	2013 Feb 15	H245+75	2013 Feb 22
L244+75	2013 Apr 8								

sen to span the range of observed flux densities in the survey. For the multi-band analysis we additionally drew source spectral indices from a Gaussian distribution with mean -0.7 and standard deviation 0.35 , and considered the flux density to be at a reference frequency in the middle of the band (135 MHz for HBA, 50 MHz for LBA). A suitable number of simulated sources were then added at random positions to the residual maps for each band. For the multi-band analysis, we constructed a detection image by averaging the individual bands (in the case of the HBA data, this was done by using residual images without beam correction, taking account of the beam correction factor by scaling the input fluxes) in order to mimic as closely as possible the process used in cataloging. Finally, PyBDSM was used to attempt to recover the simulated sources from the resulting image, taking

care to use exactly the same parameters as applied in the cataloging: a source was deemed to have been recovered if PyBDSM detected a source within 1 arcmin of the input position with a flux density that matched to within 10σ , where σ is the flux density error returned by PyBDSM. (In practice positions normally matched to within less than one pixel.) This process gave a list of matched and unmatched sources, which, after repeating several times to improve the statistics, could be used to estimate the survey completeness.

Results are shown in Fig. 13. This figure shows cumulative completeness curves, i.e. it gives the completeness for sources above the flux limit plotted. We see that the HBA catalog is expected to be 90% complete above 100 mJy , and 99% complete by around 200 mJy at a mid-band reference frequency of 135

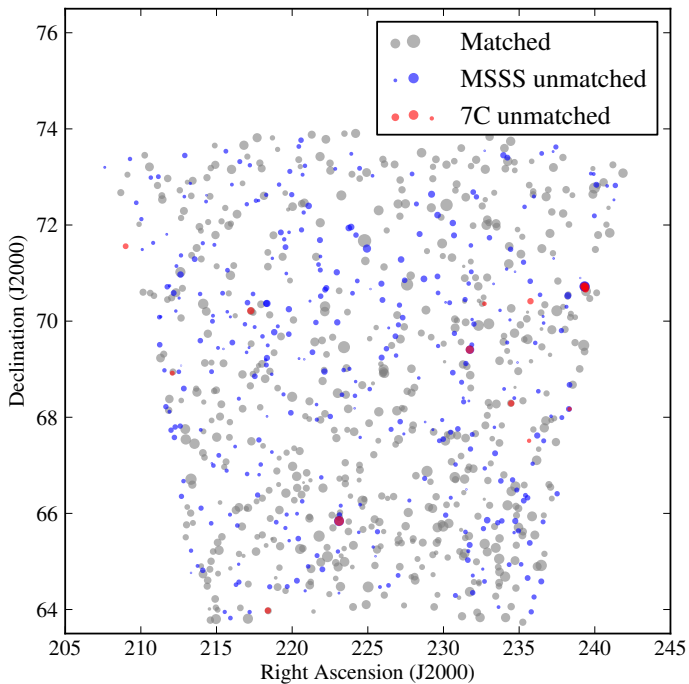


Fig. 15. Comparison of 7C and MSSS cataloged sources in the MVF.

MHz; the cataloging process using the averaged detection image gives, as expected, a catalog which is roughly a factor $\sqrt{8}$ more sensitive than those derived for the individual bands. The LBA catalog has a much higher completeness threshold of 0.55 Jy (90% complete) or 0.80 Jy (99% complete) at a reference frequency of 50 MHz.

We emphasise that these completeness curves are for point sources only (though at the resolution used that includes nearly all real sources) and that the process assumes that the beam is well modelled as a Gaussian and that residual images are free from real structure, which are good assumptions for the HBA images but much less so for the LBA. We also assume that there are no relative flux scale offsets within the LBA and HBA bands. Any departures from these assumptions will tend to make the real catalogs less complete than indicated by the completeness curves. At present we regard the HBA curves as reliable, but the LBA curves should be taken as indicative only.

Finally, a by-product of this simulation process is a test of the reliability of source flux densities as extracted with PyBDSM. We show a representative plot in Fig. 14. It can be seen that PyBDSM recovers the flux density very accurately. A few sources at low flux densities are found to have significantly (a factor of a few) high flux densities relative to the input values; we attribute this to confusion (i.e. there is some overlap with a nearby bright source which is not completely deconvolved by PyBDSM). As the right-hand panel of Fig. 14 shows, however, such sources are a very small fraction of the total.

5.2. Comparison with other catalogs

5.2.1. HBA

The HBA MSSS catalog can be compared directly to the 151-MHz 7C survey (Hales et al. 2007). 7C has a resolution of 70×70 cosec(δ) arcsec at a frequency of 151 MHz, and covers 1.7 sr of the northern sky, including the area of the MSSS described here.

We filtered the full 7C catalog⁷ to produce a catalog within the 100-deg² of the field described in this paper, containing 607 7C sources. The completeness limit for 7C in this part of the sky is about 400 mJy, and about 248 7C sources lie above this completeness limit. We would expect essentially all of these to be detected by MSSS since, as noted in Section 5.1, the MSSS is 99% complete to 200 mJy at 135 MHz. The rms noise on the 7C images is about 30 mJy, while the noise on the single-band HBA images is generally less than 20 mJy, and so in general we expect MSSS to go deeper than 7C. Indeed, after filtering out cataloged sources with poorly constrained positions and those without measured 151-MHz flux densities, there are 1193 MSSS sources in the area of interest, nearly a factor 2 more than in 7C.

We cross-matched the 7C and MSSS catalogs by combining the positional errors of each pair of sources in quadrature and finding the maximum-likelihood 7C match for each MSSS object, bearing in mind that the distribution of offsets is a Rayleigh distribution; we imposed a threshold on the acceptable maximum likelihood, determined by inspection of the matching results, to reject spurious matches. This method makes optimal use of the known positional errors. A total of 592 sources matched between the two catalogs, with a mean positional offset of 7.8 ± 0.7 and -0.8 ± 0.3 arcsec in RA and Dec respectively. Thus the vast majority of sources in the 7C catalog are successfully cross-matched with MSSS sources.

It is useful to look at the positions and fluxes of matched and unmatched sources (Fig. 15). We see that most unmatched sources are faint MSSS sources, which is just a consequence of the fact that MSSS is more sensitive than 7C over most of the sky area. The very few unmatched 7C sources are almost all positionally almost identical to MSSS sources of similar brightness, which means that these are almost certainly the same sources with positions that differ by too much for the algorithm to consider them to match. At least some such errors would be expected given the apparent systematic positional offset between the two catalogs; other sources of unmodelled positional uncertainty include the slightly higher resolution of the 7C survey.

Finally, we can consider the flux scales of the two catalogs. Here we consider only the subsample of the catalog above the 7C completeness limit of 400-mJy, since the fluxes of parts of the catalog where the samples are not complete will tend to be biased high. There is an excellent correlation (Fig. 16) between the flux densities from the two samples. Very few sources have much larger total fluxes in 7C compared to MSSS, but these differences are not present in the peak flux analysis, and so must arise from differences in the algorithms for fitting to extended sources in the two surveys. We see that there is a slight but clearly significant difference in both the peak and integrated flux densities in the 7C and MSSS catalogs, in the sense that the MSSS flux densities are systematically high by about 10% (total flux) or 9% (peak flux). Both surveys should be tied to the flux scale of Roger et al. (1973), so in principle we would not expect this systematic difference. In practice, the difference appears to be likely due to different assumptions about the flux density of 3C 295, the reference flux calibrator for almost all the MSSS observations, which seems likely to have been the primary flux calibrator for the 7C observations as well given the RA of the field McGilchrist et al. (1990). The 7C catalog uses the 6C flux density of this object, 89.8 Jy, whereas the 150-MHz flux density interpolated from the fits of Scaife & Heald (2012) is 97.7 Jy, giving the correct magnitude and direction of the flux density discrepancy. Indeed, the

⁷ Available electronically from <http://www.mrao.cam.ac.uk/facilities/surveys/7c/>

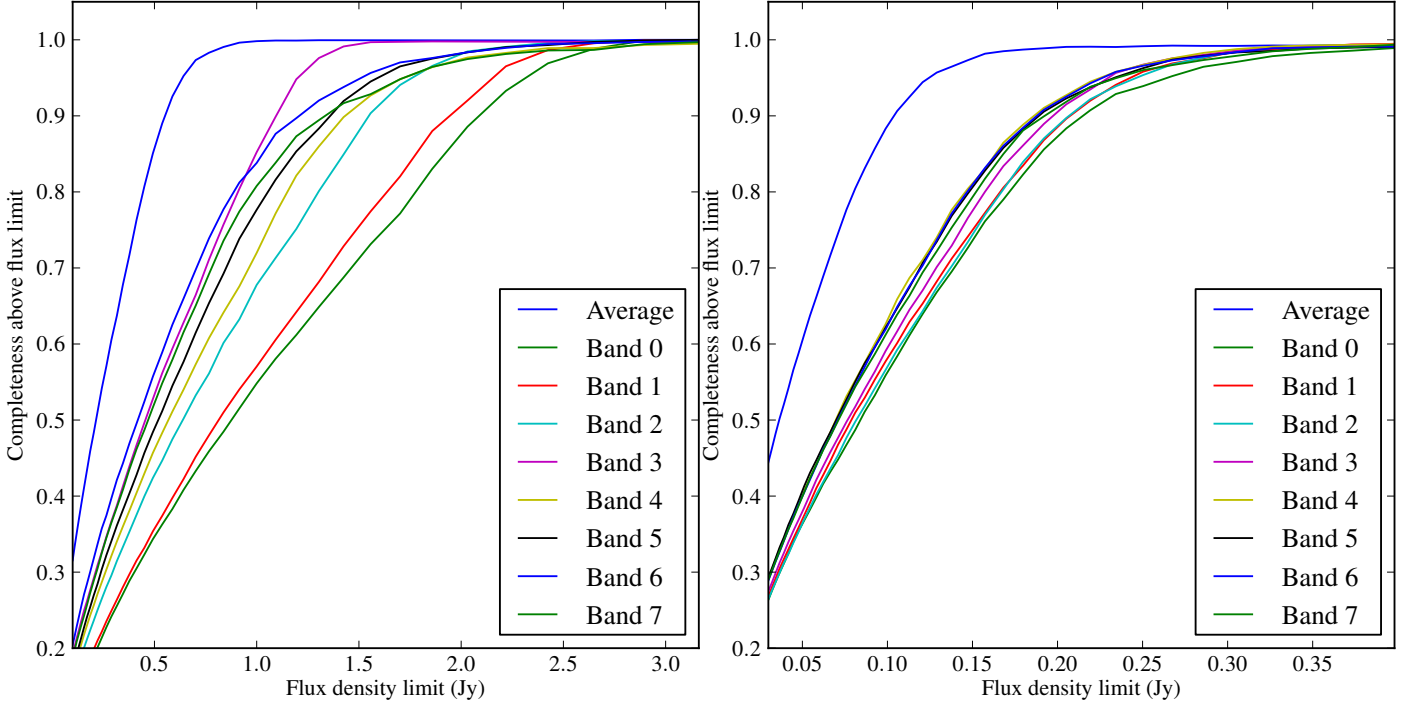


Fig. 13. Results of completeness simulations for LBA (left) and HBA (right). Curves show the cumulative completeness for the individual frequencies in the LBA and HBA and for their combination at a nominal reference frequency of 50 and 135 MHz respectively.

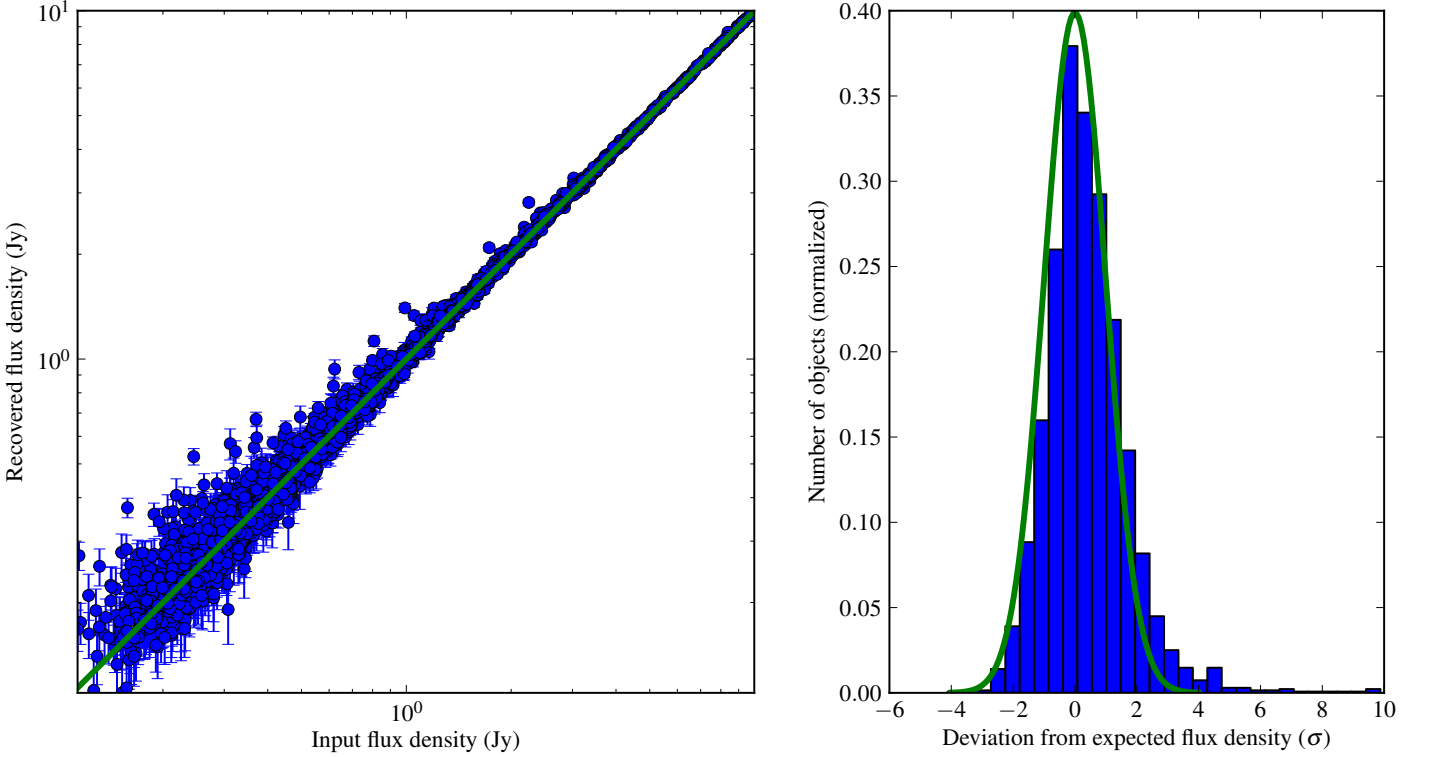


Fig. 14. Comparison of input and output model source flux densities for one band of the HBA (left) and histogram of the deviation from the expected value (right). The green line on the left shows the line of equality, on the right the expected normal distribution if the fluxes are simply affected by the noise estimated from the fit.

150-MHz flux density of 3C 295 appears anomalously low on the flux plot of Scaife & Heald, compared to, e.g., the 178-MHz 3CRR flux density. We are therefore confident in the flux scale and flux recovery in the catalog: further investigation of the true flux density of 3C 295 at HBA frequencies would be desirable.

5.2.2. LBA

LBA comparisons are restricted by the relatively small number of cataloged sources with low-frequency flux densities. However, we have compared the MSSS MVF with the 8C at 38 MHz and the VLSS at 74 MHz in the same way as in the previ-

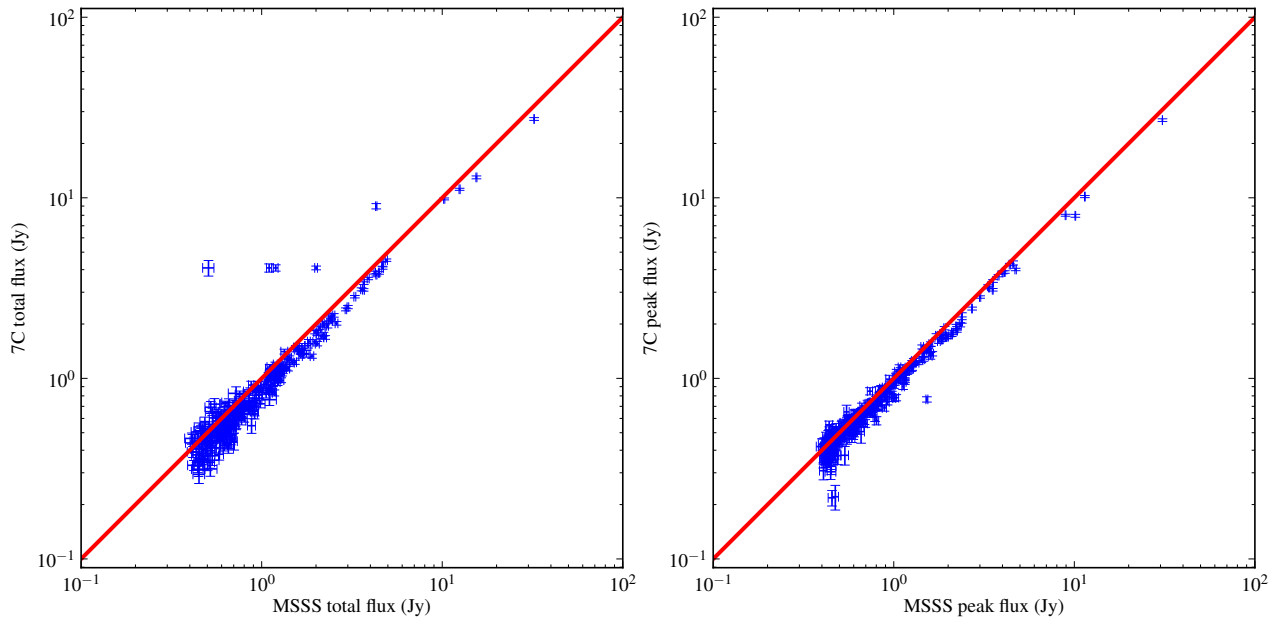


Fig. 16. Comparison of total (*left*) and peak (*right*) flux densities for bright sources in the MSSS and 7C surveys.

ous section. We find that there are a similar number of MSSS and 8C sources in the field, but only around 80% of MSSS sources (above ~ 0.8 Jy at 50 MHz, the 99 per cent completeness level) have a counterpart in 8C, and similarly there are 8C sources with no MSSS counterpart. The 8C flux densities are higher than the MSSS ones by about 14%, with significant scatter. By contrast, the VLSS appears to go slightly deeper than MSSS, but at the 99% completeness level nearly all (94%) of the MSSS sources have VLSS counterparts, with a good agreement between peak fluxes – the VLSS sources are brighter by about 3%, with little scatter. A detailed comparison with these catalogs is deferred until a larger field is available.

6. Scientific capability

To assess how MSSS compares with other existing, ongoing, and future surveys, we list key parameters in Table 4. The survey parameters illustrate that MSSS is complementary to existing catalogs, with potential for even better image quality with followup reprocessing steps.

The values for sensitivity and resolution are shown graphically in Figure 17. The sensitivity panel shows that sources with typical spectral indices will be detected in both WENSS and MSSS. Steep spectrum sources detected in NVSS will also be recovered in MSSS. Therefore, the sensitivity of MSSS make it interesting in terms of comparison with other all-sky surveys. The study of steep spectrum sources (e.g. radio galaxies and diffuse synchrotron sources) in particular will be strongly enhanced by MSSS. It is clear from Figure 17, however, that a larger LOFAR array should be processed in order for the MSSS angular resolution to be competitive with the other existing surveys.

6.1. Long baselines

International stations are always included in the LBA observations, but not in the HBA observations for the reasons described in § 2.2. A long-baseline working group is planning to use MSSS data as part of a survey for long-baseline calibrators (see also Moldon 2014), and to provide initial images for the brightest

sources. Test processing rounds have demonstrated that higher angular resolution imaging is feasible despite the sparse uv coverage. HBA images at $5 - 30''$ resolution (using the outer Dutch remote stations) have been successfully produced. Efforts toward a large-scale reprocessing of the MSSS data to produce a high-resolution catalog are in an early phase at the time of writing.

An example of higher resolution imaging of MSSS data is presented in Figure 18. The MSSS-HBA observations of field H063+39 were reprocessed using an automated self-calibration loop that has been developed as part of an overall upgrade to the TIP (see § 3.4). This scheme performs a progressively higher angular resolution sequence of source finding, phase calibration and imaging. Here, we have performed 8 iterations to achieve a final image resolution of $42''$ after averaging over 5 bands (cf. the initial resolution of MSSS images, $2.5'$ from baselines ≤ 2 k λ ; see § 3.4.1). While the data provide the capability for still higher angular resolution, our aim here is to demonstrate image quality comparable to existing higher frequency radio surveys. We have selected 3 sources from the field of view that are resolved in the high resolution MSSS image: 3C 111 and two double-lobed radio galaxies (4C +39.13 and 4C +37.10). Through comparison with the NVSS images of the same objects it is clear that the morphology is properly reproduced in the reprocessed MSSS data, at an order of magnitude lower frequency.

6.2. Transients and variable sources

There are multiple aspects of the MSSS survey that are useful for conducting transient searches. First, the 9 (2) snapshots in LBA (HBA) mode allow a limited variability and transient capability. Furthermore, in LBA mode a single subband beam is always placed on the north celestial pole (NCP), enabling transient monitoring on longer timescales (albeit with reduced sensitivity). A full description of the NCP transient monitoring program, and the first low-frequency transient identified therein, is presented in a companion paper (Stewart 2014).

MSSS is also expected to be useful to detect pulsars that are highly scattered to a degree that causes the pulse profile to be indistinguishable in beamformed observations (see Stappers

Table 4. Nominal MSSS parameters and comparison with other surveys

Survey	Frequency	Sensitivity	Resolution	Area
MSSS-LBA	30 – 78 MHz	$\lesssim 50$ mJy beam ⁻¹	$\lesssim 150''$	20,000 □° ($\delta > 0^\circ$)
8C	38 MHz	200 – 300 mJy beam ⁻¹	$4.5' \times 4.5'$ csc(δ)	3,000 □° ($\delta > +60^\circ$)
VLSS	74 MHz	100 mJy beam ⁻¹	80''	30,000 □° ($\delta > -30^\circ$)
MSSS-HBA	120 – 170 MHz	$\lesssim 10 - 15$ mJy beam ⁻¹	$\lesssim 120''$	20,000 □° ($\delta > 0^\circ$)
7C	151 MHz	20 mJy beam ⁻¹	$70'' \times 70''$ csc(δ)	5,500 □° (irregular coverage)
TGSS	140 – 156 MHz	7 – 9 mJy beam ⁻¹	20''	32,000 □° ($\delta > -30^\circ$)
WENSS	330 MHz	3.6 mJy beam ⁻¹	$54'' \times 54''$ csc(δ)	10,000 □° ($\delta > +30^\circ$)
NVSS	1400 MHz	0.45 mJy beam ⁻¹	45''	35,000 □° ($\delta > -40^\circ$)

Note. Sensitivity and resolution values for the MSSS survey components are upper limits corresponding to images produced with baselines shorter than 3 k λ . Longer baselines are included in the observations as a matter of course, enabling re-processing toward the production of an updated, higher angular resolution catalog.

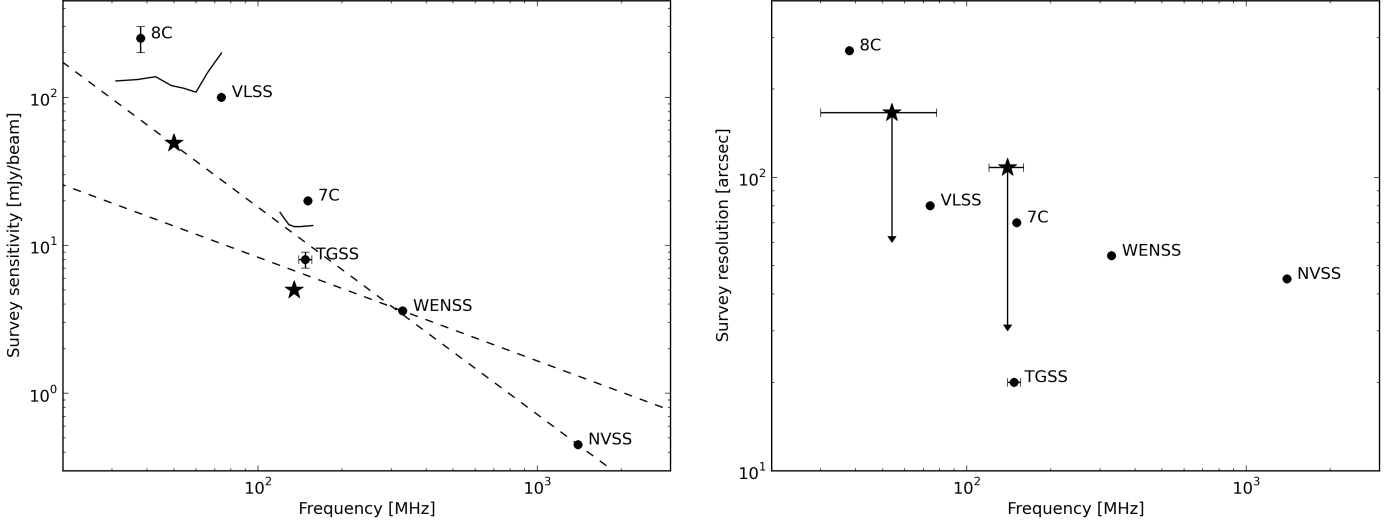


Fig. 17. Comparisons between MSSS sensitivities (*left*) and resolutions (*right*) with those of other existing radio surveys as summarized in Table 4. In the lefthand panel, dashed lines indicate representative spectral indices of $\alpha = -0.7$ and $\alpha = -1.4$. The solid black lines illustrate the frequency dependence of the sensitivity in the 8 bands in each of the LBA and HBA survey segments, while the black stars show the frequency-averaged sensitivity demonstrated in § 5. In the righthand panel, the downward-pointing arrows indicate that the angular resolution of the initial MSSS catalog is limited with respect to the capabilities of the visibility data. Processing the full array will improve the survey performance.

et al. 2011, for a description of the beamformed pulsar observing method). In imaging observations, the total flux density from the pulsar will still be visible, permitting study of the low-frequency spectral behavior of such objects.

6.3. Magnetism

A magnetism working group is planning to perform RM Synthesis (Brentjens & de Bruyn 2005) on MSSS data in order to search for polarized sources, primarily Galactic (pulsars and diffuse foreground emission; see Jelić et al. 2014), but with hopes of detecting polarized AGN (e.g., Mulcahy et al. 2014) as well.

A polarization survey based on MSSS data will be uniquely powerful at these frequencies; with the full achievable angular resolution and sensitivity over the entire survey area, it will help greatly in furthering our understanding of polarization at low frequencies. The HBA component of MSSS provides an excellent Faraday resolution of ≈ 1.3 rad m⁻² and a maximum Faraday Depth of approximately 330 rad m⁻². The Rotation Measure Spread Function (RMSF), which displays the response to simple polarized sources using all 8 HBA bands together from MSSS, can be seen in Figure 19. Initial tests of the polarization recoverable through MSSS have already been performed. Polarized

Galactic foreground emission from the Fan region has been detected, matching structures seen in previous observations with WSRT (e.g., Iacobelli et al. 2013). In addition to this, the highly polarized pulsar PSR J0218+4232 with a known Faraday depth of -61 rad m⁻² (Navarro et al. 1995) was detected at the correct Faraday depth after correction for ionospheric Faraday rotation (Sotomayor-Beltran et al. 2013). This demonstrates that an accurate polarization survey of the Galactic foreground and extra galactic background sources is feasible with MSSS-HBA. This effort will be presented in a future paper.

6.4. Individual extragalactic and Galactic targets

The key unique aspect of MSSS is its intrinsic broadband nature that enables study of the spectral properties in various classes of sources. The primary sources of interest include galaxy clusters, star-forming galaxies, AGN, and supernovae, among others. Several working groups have been formed to investigate preliminary samples of targets and determine their low frequency spectra. Particular scientific questions to be addressed include the spectral properties of galaxy cluster halos and the search for previously unknown diffuse emission; the spectral behavior of nearby star-forming galaxies and the prevalence of spectral turnovers at low frequencies; characterization of giant radio

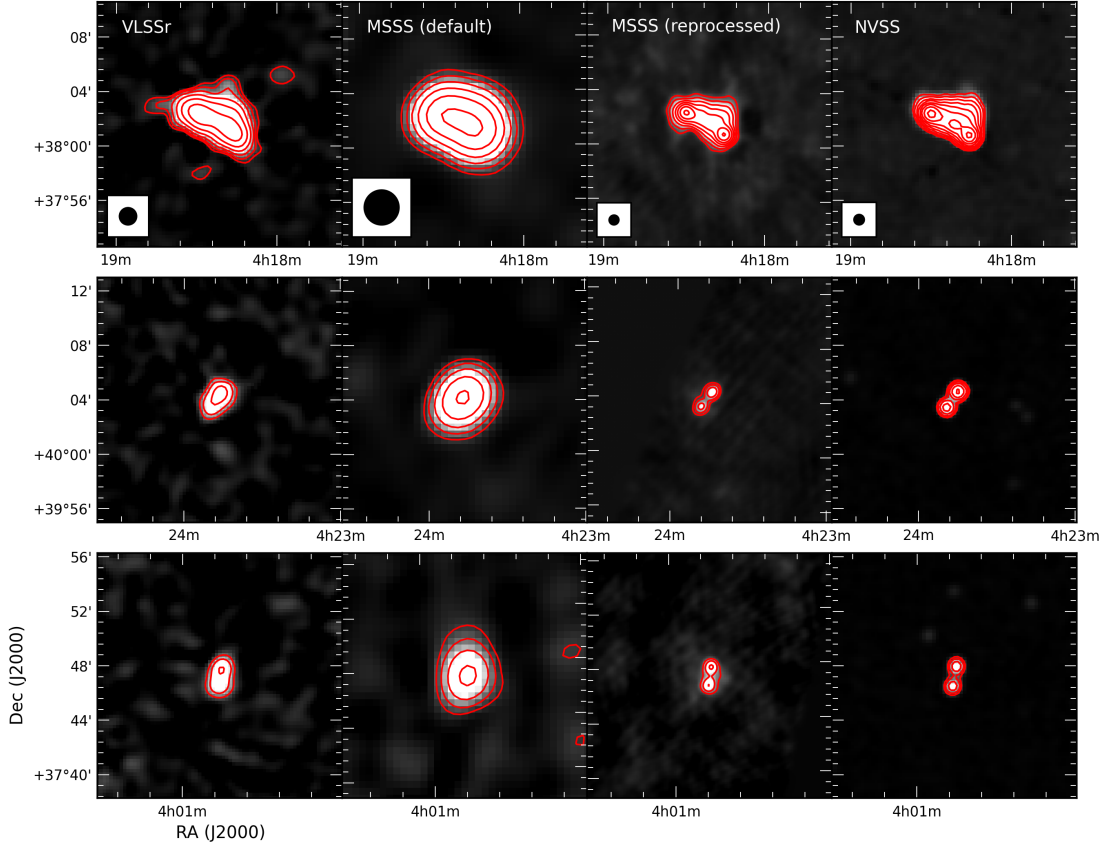


Fig. 18. Images of three sources, one per row, identified in the field of H063+39. The sources are 3C 111 (*top*), 4C +39.13 (*middle*) and 4C +37.10 (*bottom*). In each row the left panel displays the VLSSr image (resolution $75''$); the next two rows display MSSS images at $2.5'$ and $42''$ resolution (see § 6.1), and the right panel displays the NVSS image (resolution $45''$). The beamsizes for each column is plotted in the top row. Contour levels begin at 0.6 Jy beam^{-1} for VLSSr; 1, 0.2 and 0.2 Jy beam^{-1} for low-resolution MSSS; 0.2, 0.15 and 0.1 Jy beam^{-1} for high-resolution MSSS; and $0.02 \text{ Jy beam}^{-1}$ for NVSS. Contours increase by multiples of 2 in all frames.

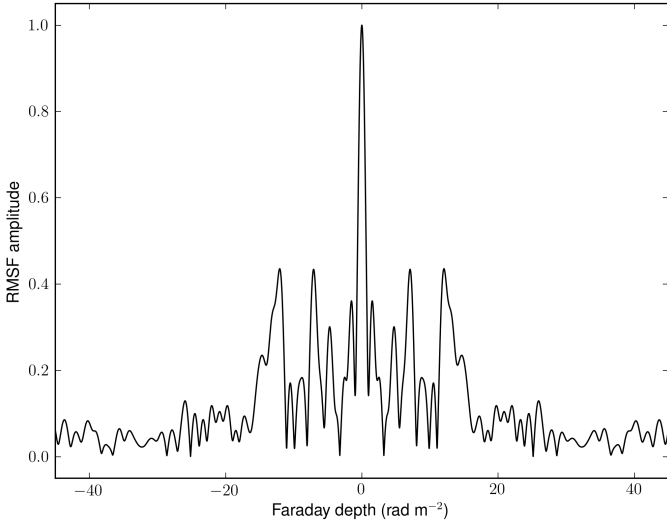


Fig. 19. Rotation measure spread function provided by MSSS, considering the combination of all 8 HBA bands.

galaxies (GRGs) and the search for previously unknown objects; and the search for new supernova remnants and Pulsar Wind Nebulae (PWNe).

7. Summary and outlook

We have presented the motivation and setup of the Multifrequency Snapshot Sky Survey (MSSS), a groundbreaking new radio continuum survey being performed with LOFAR. The primary design goal is a moderate angular resolution ($\sim 2'$), moderate depth ($\sim 10 \text{ mJy beam}^{-1}$) but intrinsically broadband survey to populate the initial LOFAR source database that will be used for calibration purposes in forthcoming deeper observations. The survey is also fertile ground for new scientific research into the source population of the low-frequency sky, and in particular uniquely enables the study of the spectral characteristics of the brighter sources detected by MSSS.

The quality of the forthcoming initial MSSS data release has been illustrated within the MSSS Verification Field (MVF), a representative 100 square degree area centered at $(\alpha, \delta) = (15^h, 69^\circ)$. We find that the survey area studied here is 90% complete above 100 mJy in the HBA with angular resolution $108''$, and above 550 mJy in the LBA with $166''$ resolution. Source positions and fluxes match well with existing radio surveys in these frequency ranges, albeit with possible small flux scale offsets that require confirmation over a larger sample area.

Subsequent MSSS data releases are anticipated, with the potential for improved multi-directional calibration (essential especially for the LBA portion of MSSS) and higher angular resolution imaging. We are also actively pursuing a number of science projects centered around the MSSS catalog, as outlined in § 6. These results will be presented in future papers.

Acknowledgements. LOFAR, the Low Frequency Array designed and constructed by ASTRON, has facilities in several countries, that are owned by various parties (each with their own funding sources), and that are collectively operated by the International LOFAR Telescope (ILT) foundation under a joint scientific policy. We acknowledge financial support from the BQR program of Observatoire de la Côte d’Azur and from the French A.S. SKA-LOFAR. C.F. acknowledges financial support by the “*Agence Nationale de la Recherche*” through grant ANR-09-JCJC-0001-01. AR, **etc** acknowledge support from the European Research Council via Advanced Investigator Grant no. 247295. R.P.B., J.B., A.J.S., M.P., **etc** were funded by a European Research Council Advanced Grant 267697 “4 Pi Sky: Extreme Astrophysics with Revolutionary Radio Telescopes”.

References

- Bhatnagar, S., Cornwell, T. J., Golap, K., & Uson, J. M. 2008, *A&A*, 487, 419
- Brentjens, M. A. & de Bruyn, A. G. 2005, *A&A*, 441, 1217
- Bridle, A. H. & Schwab, F. R. 1999, in *Astronomical Society of the Pacific Conference Series*, Vol. 180, *Synthesis Imaging in Radio Astronomy II*, ed. G. B. Taylor, C. L. Carilli, & R. A. Perley, 371
- Briggs, D. S. 1995, PhD thesis, The New Mexico Institute of Mining and Technology
- Burnham, K. P. & Anderson, D. R. 2002, *Model selection and multi-model inference: a practical information-theoretic approach* (Springer)
- Carilli, C. L. & Rawlings, S. 2004, *New A Rev.*, 48, 979
- Cohen, A. 2004, *Long Wavelength Array Memo*, 17, 1
- Cohen, A. S., Lane, W. M., Cotton, W. D., et al. 2007, *AJ*, 134, 1245
- Condon, J. J., Cotton, W. D., Fomalont, E. B., et al. 2012, *ApJ*, 758, 23
- Cornwell, T. J., Golap, K., & Bhatnagar, S. 2008, *IEEE Journal of Selected Topics in Signal Processing*, 2, 647
- Demleitner, M. 2014, in *Astronomical Society of the Pacific Conference Series*, Vol. 485, *Astronomical Society of the Pacific Conference Series*, ed. N. Manset & P. Forshay, 309
- Hales, S. E. G., Riley, J. M., Waldram, E. M., Warner, P. J., & Baldwin, J. E. 2007, *MNRAS*, 382, 1639
- Hales, S. E. G., Waldram, E. M., Rees, N., & Warner, P. J. 1995, *MNRAS*, 274, 447
- Hamaker, J. P., Bregman, J. D., & Sault, R. J. 1996, *A&AS*, 117, 137
- Heald, G., McKean, J., Pizzo, R., et al. 2010, *ArXiv e-prints*
- Hopkins, A. M., Miller, C. J., Connolly, A. J., et al. 2002, *AJ*, 123, 1086
- Hurley-Walker, N., Morgan, J., Wayth, R. B., et al. 2014, *ArXiv e-prints*
- Iacobelli, M., Haverkorn, M., Orrú, E., et al. 2013, *A&A*, 558, A72
- Intema, H. T., van der Tol, S., Cotton, W. D., et al. 2009, *A&A*, 501, 1185
- Jauncey, D. L. 1975, *ARA&A*, 13, 23
- Jelić, V., de Bruyn, A. G., Mevius, M., et al. 2014, *A&A*, 568, A101
- Lane, W. M., Cotton, W. D., Helmboldt, J. F., & Kassim, N. E. 2012, *Radio Science*, 47, 0
- McGilchrist, M. M., Baldwin, J. E., Riley, J. M., et al. 1990, *MNRAS*, 246, 110
- McKean, J., Ker, L., van Weeren, R. J., et al. 2011, *ArXiv e-prints*
- McKean, J. *et al.* 2015, *A&A*, in prep
- Moldon, J. *et al.* 2014, *A&A*, in prep
- Mulcahy, D. D., Horneffer, A., Beck, R., et al. 2014, *A&A*, 568, A74
- Navarro, J., de Bruyn, A. G., Frail, D. A., Kulkarni, S. R., & Lyne, A. G. 1995, *ApJ*, 455, L55
- Offringa, A. R., de Bruyn, A. G., Biehl, M., et al. 2010, *MNRAS*, 405, 155
- Offringa, A. R., de Bruyn, A. G., Zaroubi, S., et al. 2013, *A&A*, 549, A11
- Rees, N. 1990, *MNRAS*, 244, 233
- Rengelink, R. B., Tang, Y., de Bruyn, A. G., et al. 1997, *A&AS*, 124, 259
- Roger, R. S., Costain, C. H., & Bridle, A. H. 1973, *AJ*, 78, 1030
- Röttgering, H., Afonso, J., Barthel, P., et al. 2011, *Journal of Astrophysics and Astronomy*, 32, 557
- Sault, R. J., Teuben, P. J., & Wright, M. C. H. 1995, in *Astronomical Society of the Pacific Conference Series*, Vol. 77, *Astronomical Data Analysis Software and Systems IV*, ed. R. A. Shaw, H. E. Payne, & J. J. E. Hayes, 433
- Scaife, A. M. M. & Heald, G. H. 2012, *MNRAS*, 423, L30
- Sotomayor-Beltran, C., Sobey, C., Hessels, J. W. T., et al. 2013, *A&A*, 552, A58
- Stappers, B. W., Hessels, J. W. T., Alexov, A., et al. 2011, *A&A*, 530, A80
- Stewart, A. J. *et al.* 2014, *MNRAS*, in prep
- Szalay, A. S., Connolly, A. J., & Szokoly, G. P. 1999, *AJ*, 117, 68
- Tasse, C., van der Tol, S., van Zwieten, J., van Diepen, G., & Bhatnagar, S. 2013, *A&A*, 553, A105
- Tingay, S. J., Goeke, R., Bowman, J. D., et al. 2013, *PASA*, 30, 7
- van der Tol, S., Jeffs, B. D., & van der Veen, A.-J. 2007, *IEEE Transactions on Signal Processing*, 55, 4497
- van Haarlem, M. P., Wise, M. W., Gunst, A. W., et al. 2013, *A&A*, 556, A2